Boundary Layer Flashback of Turbulent Premixed Hydrogen/DNG/Air Flames produced by a Bunsen Burner

Thesis report

TU Delft

Tim Lambers - 4971299
Supervisors
Prof.dr.ir. Sikke Klein
Dr.ir. Mark Tummers

March 17, 2021

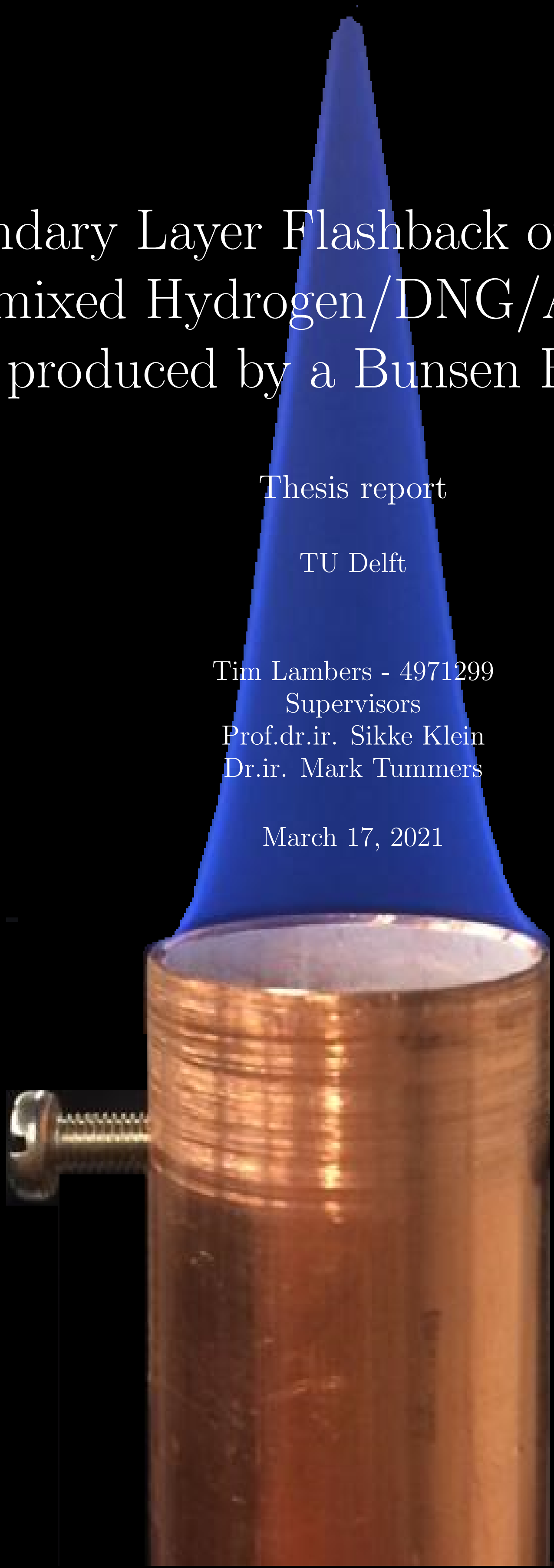

Abstract

Due to the growing energy demand and global warming renewable energy is currently of interest. To deal with the production intermittency of renewable energy, energy might be stored in hydrogen. Hydrogen can be converted into electricity with a fuel cell or by combusting hydrogen in a gas turbine. Gas turbines are more suitable for large power outputs. Large power outputs require large volumetric flow rate through the gas turbine. The large volumetric flow rate causes high gas velocities and results in a turbulent flow. Using hydrogen instead of natural gas as energy resource changes the stable operating regime and increases flame flashback propensity. Current studies done at the Technical University of Munich and the Technical University of Delft suggest flame confinement, burner wall temperature and velocity fluctuations are vital to the flashback process. Despite the recent studies flashback is yet not completely understood.

This research focuses on premixed turbulent hydrogen and hydrocarbon combustion to further investigate the possibilities of using hydrogen in a gas turbine. The aim of this research is to gain more insight in the flashback process by varying velocity fluctuations while keeping the bulk velocity constant. The first objective is to gain insight in the relation between bulk velocity at flashback and velocity fluctuations. The second objective is to gain insight in the relation between bulk velocity at flashback and low velocity streaks upstream the flame front. The third research objective is to gain insight in the relation between flame front, boundary layer obstruction and bulk velocity at flashback.

All experiments were conducted with a Bunsen burner. A screw, acting as boundary layer obstruction, was placed below the burner rim to locally disturb the flow. The influence of the local disturbance on bulk velocity at flashback was investigated by mapping flashback propensity and by examining non-reacting and reacting pipe flow with planar Particle Image Velocimetry (PIV). The fuel compositions studied in this research are DNG, hydrogen and mixtures containing 20, 40, 60 or 80 volumetric percentage H_2.

The flashback maps show that bulk velocity at flashback increases with obstruction height for all gas mixtures. The obstruction height is the height from burner wall to screw tip. The results obtained through the non-reacting field experiment confirmed that the flow was fully-developed and turbulent. Furthermore, the results showed that obstruction height locally increased velocity fluctuations. The average velocity downstream the obstruction slightly decreased with increasing obstruction height. The reacting field was examined during flashback and during stable operation to relate flashback propensity and time-averaged flow characteristics with statistical analysis. The results showed flame front axial distance from the burner rim decreases with increasing obstruction height, indicating that a flame produced by a burner with boundary layer obstruction is more prone to flashback. The flow characteristics just upstream the flame front were analyzed because once the conditions upstream the flame front are suitable, flashback occurs.

A flashback prediction model developed at the TU Munich was modified to account for the obstruction height. The modelled results indicate that, in an unconfined set-up, flashback might be described with time-averaged flow characteristics and that the turbulent burning velocity is strongly correlated to the bulk velocity at flashback. Histograms of the instantaneous velocity showed that obstruction height has no influence on low velocity streaks and thus it seems low velocity streaks are not dominant in the flashback process of

premixed unconfined flames. The absence of low velocity streaks for different obstruction heights indicates that flashback of unconfined flames is a different process than flashback of confined flames.

Acknowlegdements

First of all I want to thank Mark and Sikke for their time and help during this research. I want to thank Bart and Luuk for their daily support and the team-environment that they have created. I want to thank Dries, Pleuni, Gearte Nynke, Eline and Stan for listening to me and for their laughs. I want to thank my grandmother for being proud of me. As a matter of fact, the love and support of my whole family is very much needed and appreciated. Therefore, I would like to conclude by thanking them for everything.

Contents

Nomenclature

Abbreviation

AFT	Adiabatic flame temperature
BL	Boundary layer
BLF	Boundary layer flashback
CIVB	Combustion induced vortex breakdown
DL	Darrieus-Landau instability
DNG	Dutch natural gas
RANS	Reynolds averaged Navier-Stokes
RMS	Root-Mean-Square
STD	Standard deviation

Greek symbols

α	Thermal diffusivity (m^2s^{-1})
α_f	Flame cone angle (°)
δ_{ph}	preheat zone (m)
δ_q	Quenching distance (m)
δ_r	reaction zone (m)
δ_f	Flame thickness (m)
ϵ	Turbulent kinetic energy dissipation (m^2s^{-3})
η	Kolmogorov length scale (m)
κ	Flame stretch rate (s^{-1})
λ	Thermal conductivity ($Wm^{-1}K^{-1}$)
μ	Dynamic viscosity (Pa s)
ν	Kinematic viscosity (m^2s^{-1})
ϕ	Equivalence ratio (-)
ρ_b	Burned gas density (kgm^{-3})
ρ_u	Unburned gas density (kgm^{-3})
σ	Burned to unburned gas density ratio (-)
τ_{ch}	Chemical time scale (s)
τ_η	Kolmogorov time scale (s)

Latin symbols

A_b	Burner area (m^2)
A_f	Flame surface area (m^2)
C_α	Correction factor based on experimental flame angle (-)
c_p	Specific heat at constant pressure ($Jkg^{-1}K^{-1}$)
D	Tube outer diameter (m)
d	Tube inner diameter (m)
$\mathcal{D}$	Mass diffusivity coefficient (m^2s^{-1})
d_p	Particle diameter (m)
g_c	Critical velocity gradient (s^{-1})
h_{obstr}	Screw tip height, distance from screw tip to burner wall (m)
k	Turbulent kinetic energy (m^2s^{-2})
l_0	Turbulent integral length scale (m)
l_m	Markstein length (m)

p_n	Pressure at normal conditions (bar)
S_l	Laminar flame speed (ms^{-1})
$S_{l,s}$	Stretched laminar flame speed (ms^{-1})
S_t	Turbulent flame speed (ms^{-1})
t_0	Turbulent integral time scale (s)
T_b	Burned gas temperature (K)
T_u	Unburned gas temperature (K)
T_n	Temperature at normal conditions (K)
u'	Velocity fluctuation in axial direction (ms^{-1})
$\overline{u'u'}$	Reynolds normal stress in axial direction (m^2s^{-2})
$\overline{u'v'}$	Reynolds shear stress (m^2s^{-2})
$\overline{u}$	Mean axial velocity (ms^{-1})
u^+	Dimensionless velocity (-), $\frac{u}{u_\tau}$
u_0	Turbulent integral velocity scale (ms^{-1})
U_b	Bulk velocity (ms^{-1})
u_f	Fluid velocity (ms^{-1})
u_p	Particle velocity (ms^{-1})
u_τ	Shear velocity (ms^{-1})
U_{FB}	Bulk velocity at flashback (ms^{-1})
v'	Velocity fluctuation in radial direction (ms^{-1})
$\overline{v'v'}$	Reynolds normal stress in radial direction (m^2s^{-1})
$\overline{v}$	mean radial velocity (ms^{-1})
v_0	Turbulent integral velocity scale (ms^{-1})
v_η	Kolmogorov velocity scale (ms^{-1})
x_{FF}	Downstream location flame front (m)
y^+	Dimensionless wall normal distance (-), $\frac{u_\tau y}{\nu}$
Dimensionless numbers	
Ka	Karlovitz number (-)
Le	Lewis number (-)
Le_{mix}	Lewis number of mixture (-)
Re	Reynolds number (-)
Re_p	Particle Reynolds number (-)
Re_t	Turbulent Reynolds number (-)
Ze	Zel'dovich number (-)

1 Introduction

1.1 Relevance of this research

Energy demand is growing. The Energy Information Administration, or EIA, expects the energy demand is increased with 50% in 2050 [Kahan, 2019]. Meanwhile, temperature increases due to global warming. Since 1880 the earth's average surface temperature increased with 2 °C and the ten warmest years on record were all recorded after 1998 [Lindsey and Dahlman, 2020]. Greenhouse gases from human activities are the most significant driver of global warming [Ramanathan and Feng, 2009]. The production of greenhouse gases such as carbon dioxide and methane is related to the use of fossil fuels. The EIA reports that most fossil fuels are consumed for industrial purposes [Kahan, 2019]. Power plants convert fossil fuel to electricity. The most common energy resources used in power plants are coal and natural gas and even though natural gas is the cleanest burning and low CO_2 emission hydrocarbon [Tay-Wo-Chong et al., 2009], the available energy resources do not suffice to decrease or prevent global warming. To decrease greenhouse emissions and to deal with the finiteness of fossil fuels, emphasis is put on shifting from fossil fuels as main energy resource to renewable energy. Figure 1.1 shows the increase in the worlds renewable energy over the years.

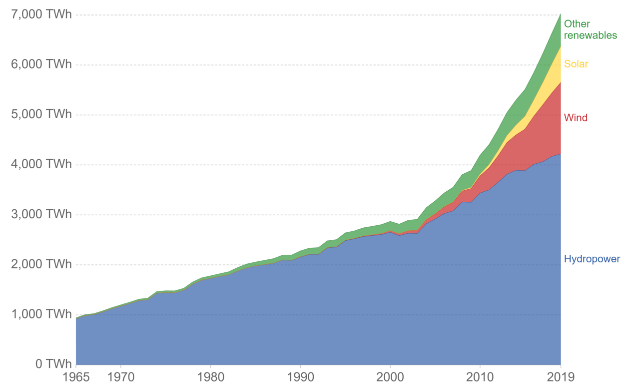

Figure 1.1: Renewable energy production from 1965 to 2019 [Richie, 2019].

The energy that is harvested directly from natural resources is called primary energy. All the world's sources of primary energy are called the world's Total Primary Energy Supply [Hanania and Donev, 2020]. In 2017, 13.5% of the world's Total Primary Energy Supply was produced with renewable energy resources [IEA, 2019].
Production of renewable energy is intermittent due to it's dependence on the environmental conditions. To cope with the intermittency of solar and wind energy sources, energy might be stored when abundant. Energy storage is one of the issues preventing the shift from fossil fuels to renewable energy because batteries that store electrical energy are heavy and consume a lot of material and space. A 'battery fuel' such as hydrogen might offer a solution to the storage problem.

Hydrogen can be converted into electricity by using a fuel cell or by combustion in a gas turbine. Fuel cells are reported to have high efficiency and to have a capacity in the range of one Megawatt [Kirubakaran et al., 2009]. Hydrogen combustion is carbon-free. Gas turbine capacity is typically in the range 1 - 400 MW and thus gas turbines offer a better solution for large scale energy conversion when compared to fuel cells. Gas turbines are able to deal with the intermittency of renewable energy due to fast start-up time [Richards, 2001].
The thermodynamic properties of hydrogen, i.e. high flame speed make it challenging to operate a gas turbine with hydrogen as energy resource. The high adiabatic flame temperature of hydrogen flames increases NOx emission and the higher flame speed could cause operating problems because the flashback propensity increases. Flashback is undesired upstream flame propagation into parts of the turbine that are not designed to hold a flame. Flashback is to be avoided because flashback would lead to material damage due to high flame temperature.
The type of flashback to occur most in gas turbine combustors is Boundary Layer Flashback (BLF). Boundary layer flashback occurs when the gas axial velocity close to the burner wall is lower than the local flame speed. Boundary layer flashback of laminar flames was first studied in 1943 by Lewis and Von Elbe, leading to the so called critical velocity gradient model. The model neglects flame-flow interaction [Lewis and von Elbe, 1943]. Recent studies published by Eichler and Hoferichter show that flashback does not occur in the viscous sublayer and that flame-flow interaction influences flashback propensity [Eichler et al., 2012] [Hoferichter et al., 2017b]. Despite the recent studies boundary layer flashback is yet not completely understood. To achieve flashback control in a gas turbine combustor, the flashback mechanism of hydrogen and hydrocarbon flames should be understood. The goal of this research is to gain insight in the dominant mechanism invoking boundary layer flashback of premixed turbulent hydrogen/DNG/air flames.

1.2 Research objectives

To gain insight in the dominant mechanism invoking flashback a mechanical obstruction was placed in the boundary layer. The obstruction locally triggered flashback and three research objectives were formulated, see the list below.

- Gain insight in the relation between turbulent velocity fluctuations and bulk velocity at flashback.
- Gain insight in the relation between low velocity streaks upstream the flame front and bulk velocity at flashback.
- Gain insight in the relation between flame front location, boundary layer obstruction and bulk velocity at flashback.

1.3 Thesis outline

Chapter 2 contains background information on premixed laminar and turbulent combustion and flashback. To gain insight in the differences between premixed laminar and turbulent combustion, information on turbulent flow is included in Chapter 2. Furthermore, Chapter 2 contains information on a flashback prediction model that was used in the present research. The experimental set-up, measuring equipment and the experiments done in the present research are introduced in Chapter 3. The experimental results are discussed and compared with the flashback prediction model in Chapter 4. Finally, all conclusions are summarized in Chapter 5.

2 Literature review

2.1 Laminar premixed combustion

2.1.1 1D premixed laminar flame

Figure 2.1 shows a schematic of a laminar premixed 1D flame. It is assumed that fuel and oxidizer are perfectly mixed and that the unburned gas reaches the flame front as a uniform flow. Unburned gas is convected into the flame front. The flame front consists of a reaction zone and a preheat zone. The laminar flame thickness is the sum of the reaction and preheat zone thicknesses. The unburned gas reaches the preheat zone first. In the preheat zone the gas temperature increases. Due to the temperature increase, the density drops and the gas velocity increases. Once the unburned gas reaches the reaction zone, chemical reactions take place and the mass fractions of the fuel and oxidizer decrease. During the chemical reactions energy is released, increasing gas temperature and velocity and decreasing density. An expression for the laminar flame thickness, δ_f, is given by:

$$\delta_f = \frac{\alpha}{S_l}, \tag{2.1}$$

where α is the thermal diffusivity and S_l is the laminar flame speed. The laminar flame speed is defined perpendicular to the flame front. The mass flux $\dot{m}$ is given by:

$$\dot{m} = \rho_u S_l A_f, \tag{2.2}$$

where A_f is the flame surface area and ρ_u is the unburned gas density. For a stationary flame front the laminar flame speed equals the unburned gas velocity, i.e.:

$$S_l = U_u. \tag{2.3}$$

Mass is conserved so for a laminar premixed 1D flame front burned and unburned gas density are related by:

$$\rho_u U_u = \rho_b U_b, \tag{2.4}$$

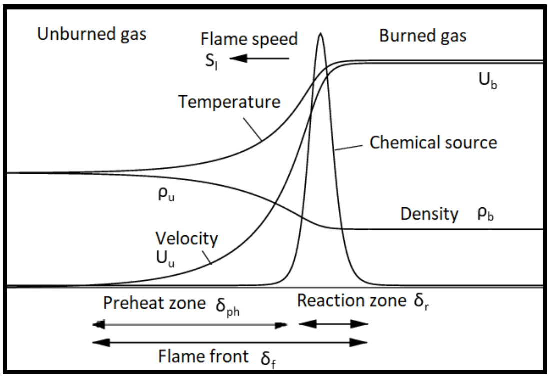

Figure 2.1: Laminar premixed 1D flame [Peters, 2000].

where U_b and ρ_b are the velocity and density of the burned gas, respectively. For a hydrogen-air mixture at stochiometric conditions, the ratio of unburned and burned gas density is $\sigma \equiv \frac{\rho_u}{\rho_b} \approx 8$.

2.1.2 Bunsen laminar flame

The flames studied in this research were produced by a Bunsen burner. Figure 2.2 shows a sketch of a premixed laminar flame produced by such a burner. In Figure 2.2 the flame front is marked by the solid black line that makes an angle α_f with the velocity of the unburned mixture, U_u. It is assumed that the unburned gas mixture reaches the flame as a uniform flow and is perfectly mixed. It is also assumed that there is a jump in gas temperature across the flame front and that the flame is shaped like a cone, defined by flame angle α_f. The laminar flame speed S_l is perpendicular to the flame front, and corresponds to the laminar flame speed of a laminar premixed 1D flame. However, the unburned gas velocity is not perpendicular to the flame. The velocities U_u and U_b are decomposed into tangential and normal components relative to the flame front. The velocity tangential component, $U_{u,t}$, remains constant across the flame and, therefore, Eq. 2.5 holds [Peters, 2000]:

$$\rho_b U_b \sin(\beta) = \rho_u U_u \cos(\alpha_f). \tag{2.5}$$

The normal velocity component increases across the flame with a factor σ corresponding to the velocity increase across a laminar premixed 1D flame. For a stationary flame, S_l is now equal to the unburned gas velocity component normal to the flame:

$$S_l = U_u \sin(\alpha_f). \tag{2.6}$$

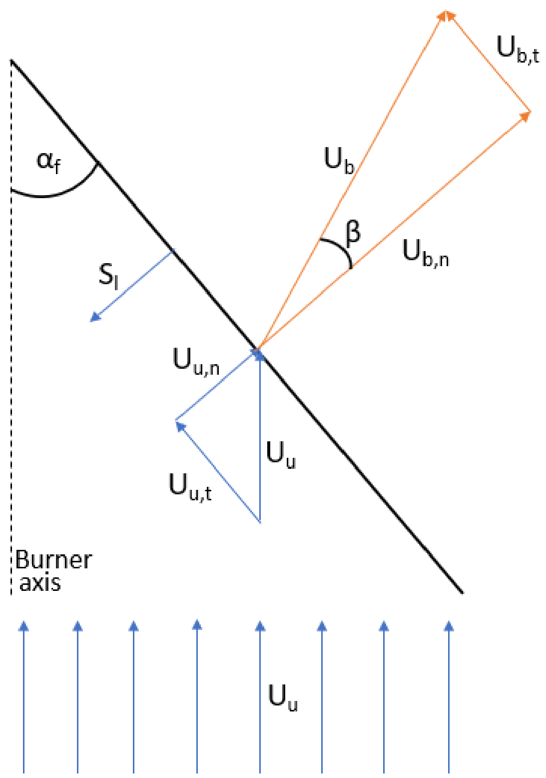

Figure 2.2: Premixed laminar flame front on a Bunsen burner.

Mass is conserved across the flame front so Eq. 2.7 holds under the mentioned assumptions on a laminar premixed flame on a Bunsen burner. The mass balance across the flame front is given by:

$$A_b \rho_u U_u = A_f \rho_b U_b \cos(\beta), \tag{2.7}$$

where A_b is the burner area and A_f is the flame surface area.

2.2 Turbulent flow

2.2.1 Flow development

The Reynolds number represents the ratio of the inertial forces over the viscous forces in a flow and turbulent flows are characterized by high Reynolds numbers. In pipe flow, the flow is generally considered turbulent when the Reynolds number (based on the pipe diameter and the bulk velocity) is $Re_D > 2300$. In practice this value might vary due to details of the pipe geometry such as surface roughness. Pipe flow is fully developed if the flow characteristics do not change in downstream direction. To ensure fully developed turbulent pipe flow the entrance length should be sufficiently large, typically 70-80 times the pipe diameter. An example of a fully developed mean velocity profile is shown in Figure 2.3.

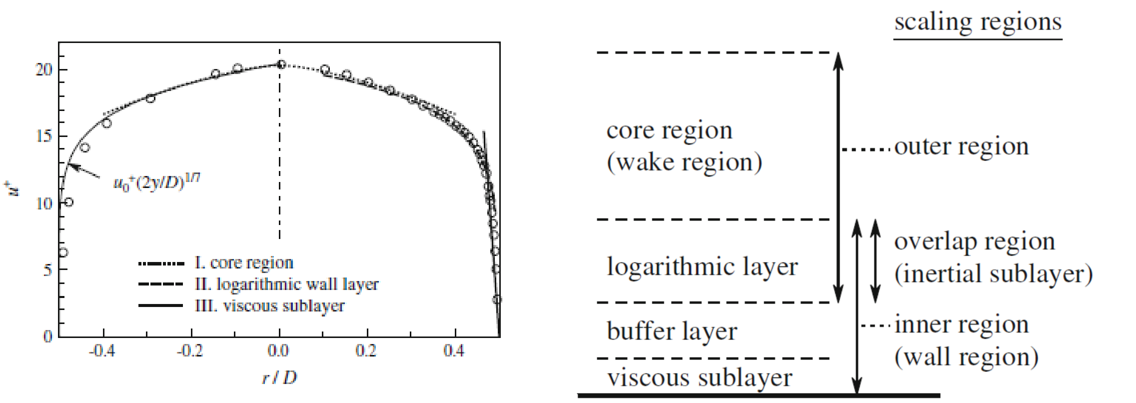

Figure 2.3: The left hand side shows the dimensionless mean velocity, u^+, as a function of dimensionless radial distance r/D from the centerline for fully developed pipe flow at Re_D = 10000. The right hand side shows a schematic of the different regions in a turbulent wall bounded flow [Nieuwstadt et al., 2015].

In Figure 2.3 the dimensionless mean velocity, u^+, is defined as:

$$u^+ = \overline{u}/u_\tau, \tag{2.8}$$

where $\overline{u}$ is the mean velocity and u_τ is the friction velocity defined as:

$$u_\tau = \sqrt{\frac{\tau_w}{\rho}}, \tag{2.9}$$

where τ_w is the wall shear stress:

$$\tau_w = \mu \frac{\partial u}{\partial y}|_{y=0}. \tag{2.10}$$

The mean velocity profile in Figure 2.3 is characterized by three regions. In the core region of the pipe the flow is turbulent and the viscous stress is negligible compared to the Reynolds stress. In the logarithmic wall layer viscous stress is of the same order as Reynolds stress and in the viscous sublayer the viscous stress dominates over the Reynolds stress. At the wall (at $|r/D| = \pm 0.5$) the velocity is zero due to the no-slip condition. In the viscous sublayer the mean velocity is given by:

$$\overline{u} = \frac{\partial \overline{u}}{\partial y}|_{y=0} y, \tag{2.11}$$

where $\overline{u}$ is the mean velocity at a given wall normal distance y. In the logarithmic layer the mean velocity is given by:

$$\overline{u} = \frac{u_\tau}{k} \ln\left(\frac{y}{y_0}\right), \tag{2.12}$$

where k is the 'Von Kármán' constant, u_τ is the wall friction velocity and y_0 is an integration constant that is representative of the wall properties. In order to match the velocity profiles in the viscous sublayer and the logarithmic layer the dimensionless wall normal distance, y^+ is introduced:

$$y^+ = \frac{u_\tau(x) y}{\nu}, \tag{2.13}$$

where ν is the kinematic viscosity. The velocity profile in the viscous sublayer holds for $y^+ < 5$ and in the logarithmic layer the velocity profile holds for $y^+ > 30$. The region $5 < y^+ < 30$ is called the buffer layer. Together, the viscous sublayer, buffer layer and the logarithmic layer form the wall region, see Figure 2.3.

2.2.2 Reynolds-averaged continuity and momentum equations

A flow is considered incompressible when the flow velocities are much smaller than the speed of sound. In the axisymmetric Bunsen burner the flow far upstream of the flame can be considered incompressible and the equation that expresses mass conservation is given by:

$$\frac{\partial u}{\partial x} + \frac{1}{r}\frac{\partial r v}{\partial r} = 0. \tag{2.14}$$

In the study of turbulent flows, instantaneous quantities (like velocity or pressure) are split into a mean and a fluctuating component. This is called Reynolds decomposition. The Reynolds decomposition of the axial velocity component, u(t), is given by:

$$u(t) = \overline{u} + u'(t), \tag{2.15}$$

where $\overline{u}$ and $u'(t)$ are the mean and fluctuating part, respectively. Applying Reynolds decomposition to the continuity equation, Eq. 2.14, followed by Reynolds averaging yields:

$$\frac{\partial \overline{u}}{\partial x} + \frac{1}{r}\frac{\partial r \overline{v}}{\partial r} = 0. \tag{2.16}$$

When the Reynolds decomposition is applied to the Navier-Stokes equations in the Boussinesq approximation and Reynolds averaging is applied, the Reynolds stress terms $\overline{u'u'}$, $\overline{v'v'}$ and $\overline{u'v'}$ appear. For example, the Reynolds averaged momentum equation for the axial direction reads:

$$\frac{\partial \overline{u}}{\partial t} + \overline{u}\frac{\partial \overline{u}}{\partial x} + \overline{v}\frac{\partial \overline{u}}{\partial r} = -\frac{1}{\rho}\frac{\partial \overline{p}}{\partial x} + \nu \nabla^2 \overline{u} - \frac{\partial \overline{u'u'}}{\partial x} - \frac{1}{r}\frac{\partial (r\overline{u'v'})}{\partial r}, \tag{2.17}$$

where the stress term $\overline{u'u'}$ is the Reynolds normal stress in axial direction and $\overline{u'v'}$ is the Reynolds shear stress. The shear stress term can be interpreted as transport in the x_j-direction of momentum per unit mass in the x_i-direction. The Reynolds stress terms add another unknown quantity to the momentum balance, resulting in a set of equations with more variables than equations. An equation for the stress terms is needed to solve the set of equations. Finding a relation for this unknown terms is referred to as the closure problem. In this research the Reynolds stresses were determined experimentally with planar Particle Image Velocimetry.

2.2.3 Kinetic energy of turbulence

Turbulence is strongly dissipative, meaning that turbulence kinetic energy is converted into heat. To get a better insight in how turbulence kinetic energy is converted into heat the equation for kinetic energy of turbulence will be used. The kinetic energy (per unit mass) of turbulent velocity fluctuations is defined by:

$$k = \frac{1}{2}\overline{u_i'^2} = \frac{1}{2}\left(\overline{u'^2} + \overline{v'^2} + \overline{w'^2}\right). \tag{2.18}$$

The transport equation for turbulent kinetic energy k is given by:

$$\frac{\partial k}{\partial t} + \overline{u}_j \frac{\partial k}{\partial x_j} = -\overline{u_i' u_j'} \frac{\partial \overline{u}_i}{\partial x_j} + \frac{\partial}{\partial x_j}\left(-\overline{u_j' k'} - \frac{1}{\rho}\overline{p' u_j'} + \nu \frac{\partial k}{\partial x_j}\right) - \epsilon. \tag{2.19}$$

The first term on the right hand side is the production term. This term represents the energy transfer from mean flow to the turbulence. The second term is called the transport term. The third term, ϵ, is the turbulence dissipation rate and it represents the rate at which turbulent kinetic energy is converted into heat. The turbulence dissipation rate, ϵ, is given by:

$$\epsilon = \nu \overline{\left(\frac{\partial u_i'}{\partial x_j}\right)^2}. \tag{2.20}$$

Under the assumption that turbulence is in equilibrium, the dissipation rate ϵ scales with the production term because the transport term cannot destroy or produce turbulence kinetic energy. The turbulence dissipation rate is then scaled according to:

$$\epsilon \sim \frac{u_0^3}{l_0}, \tag{2.21}$$

where u_0 and l_0 are the turbulent integral velocity and length scale, respectively. Turbulence is characterized by the energy cascade where large eddies break up into smaller ones and the smallest eddies dissipate into viscous heat. Eq. 2.21 relates dissipation rate which mainly takes place at the smallest turbulent scales, to the macrostructure of the turbulent flow. With this relation it is now possible to find expressions for the turbulent microscales.

2.2.4 Kolmogorov scales

The microstructure of the turbulent flow is characterized by the Kolmogorov scales. The Kolmogorov scales represent the smallest turbulent scales in the flow. The Kolmogorov scales for length η, time τ_η and velocity v_η are given by:

$$\eta = (\frac{\nu^3}{\epsilon})^{\frac{1}{4}}, \quad \tau_\eta = (\frac{\nu}{\epsilon})^{\frac{1}{2}}, \quad v_\eta = (\nu\epsilon)^{\frac{1}{4}}. \tag{2.22}$$

When the Reynolds number is defined as $Re = u_0 l_0/\nu$ combining equations 2.21 and 2.22 results in a scaling relating the turbulent microscales and macroscales as in:

$$\frac{l_0}{\eta} \sim Re^{\frac{3}{4}}, \quad \frac{t_0}{\tau_\eta} \sim Re^{\frac{1}{2}}, \quad \frac{u_0}{v_\eta} \sim Re^{\frac{1}{4}}. \tag{2.23}$$

2.3 Turbulent premixed combustion

Turbulent flow is subject to fluctuations and the same holds for turbulent flame fronts. Velocity fluctuations curve and wrinkle the flame front of a turbulent premixed flame. Due to flame wrinkling and curvature the flame front surface area and burning velocity increase [Warnatz et al., 1999]. Microstructure eddies perturb the flame front if the smallest eddies have a characteristic length smaller than the flame thickness. The Karlovitz number is defined as the ratio of the chemical time scale, τ_{ch}, and the Kolmogorov timescale, τ_η, and it is a quantitative measure to estimate the effect of turbulent eddies on the flame front. The Karlovitz number is given by:

$$Ka \equiv \frac{\tau_{ch}}{\tau_\eta}. \tag{2.24}$$

The chemical time scale is given by:

$$\tau_{ch} = \frac{\alpha}{S_l^2}, \tag{2.25}$$

where α is the thermal diffusivity and S_l is the laminar flame speed. The laminar flame thickness is $\delta_f = \alpha/S_l$. When substituting δ_f in Eq. 2.25, Eq. 2.25 reduces to:

$$\tau_{ch} = \frac{\delta_f}{S_l}. \tag{2.26}$$

The Kolmogorov timescale is given by Eq. 2.22. Rewriting Eq. 2.22 yields:

$$\tau_\eta = \frac{\eta^2}{\nu}, \tag{2.27}$$

where η is the Kolmogorov length scale and ν is the kinematic viscosity. Eq. 2.26 and 2.27 are substituted in Eq. 2.24. Under the assumption that thermal diffusivity and kinematic viscosity are equal, Eq. 2.24 reduces to:

$$Ka = \frac{\delta_f^2}{\eta^2}. \tag{2.28}$$

If $Ka < 1$, the flame front thickness is smaller than the Kolmogorov scale and the flame front is not affected by the eddies. For $Ka \geq 1$ the eddies start to perturb the flame front. The eddies enhance mixing in the flame front. If the eddies are smaller than the reaction zone thickness, $\eta < \delta_r$, the eddies are small enough to perturb the reaction zone.
The size of turbulent eddies, the degree to which the flame front is perturbed and stretched, the flame speed and the flame thickness all influence combustion, which is why turbulent premixed combustion is categorized in different flame structures. The Borghi diagram, as shown in Figure 2.4, is used to illustrate the different flame structures. The horizontal axis represents the ratio of the turbulent integral length scale and the flame front thickness. The vertical axis represents the ratio of velocity fluctuations and the laminar flame speed. Both axes are logarithmic.

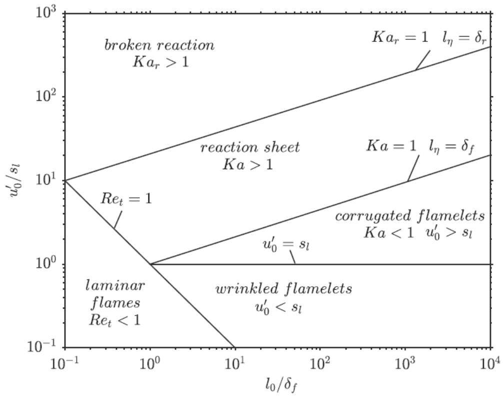

Figure 2.4: Borghi diagram of premixed flames [Peters, 2000].

In Figure 2.4, Re_t is the turbulent Reynolds number. Flames are turbulent for $Re_t > 1$ and Re_t is given by:

$$Re_t = \frac{l_0 u'}{S_l \delta_f}, \tag{2.29}$$

where l_0 and u' are the turbulence integral length scale and the velocity fluctuations at the integral length scale, respectively. In Eq. 2.29 it is assumed that the kinematic viscosity and thermal diffusivity are equal.
Above $Ka = 1$, the Kolmogorov eddies are able to perturb the flame front. In Figure 2.4 turbulent flames are separated from laminar flames by the line $Re_t = 1$. Furthermore, $Ka_\delta \equiv \delta_r^2/\eta^2$ with the reaction zone thickness being approximately one tenth of the laminar flame thickness. Thus, for $Ka_\delta < 1$, Kolmogorov eddies are able to perturb the reaction zone. For $u'/S_l < 1$, the flame front corresponds to a laminar flame front. For $u'/S_l > 1$ and $Ka < 1$, the flame structure remains laminar but the wrinkling effect is strong due to the velocity fluctuations. Although Figure 2.4 is a simplified regime map, it is a useful tool to recognize different flame structures. In Figure 2.4 it is assumed that thermal expansion effects downstream the flame front might be neglected and that flamelets are stationary [Law, 2006].

2.3.1 Turbulent burning velocity

Measurements done on turbulent burning velocity showed that it is significantly higher than the laminar burning velocity. Burning velocities increase in the turbulent regime because turbulence increases flame surface area and enhances transport. In Figure 2.5 a premixed turbulent flame front is sketched.

Figure 2.5: Premixed turbulent flame front.

In Figure 2.5 S_t is the turbulent burning velocity and $\dot{m}$ is the mass flux. The effect of turbulence on the burning velocity depends on the effect that turbulence has on the flame front. Therefore, turbulent burning velocity will be analyzed for large and small scale turbulence. Damköhler was the first to find an expression for the turbulent burning velocity. In Figure 2.5 the mass flux through the cross-sectional area, A, and the turbulent flame surface area, A_f, is equal and given by:

$$\rho_u S_l A_f = \rho_u S_t A, \tag{2.30}$$

where S_t is turbulent burning velocity. Eq. 2.30 can be rewritten to:

$$\frac{S_t}{S_l} = \frac{A_f}{A}. \tag{2.31}$$

Eq. 2.31 holds for all length scales in the inertial subrange [Peters, 2000]. Damköhler assumed that for large scale turbulence the interaction between flame front and flow field is purely kinematic in the limit of large u'/S_l, neglecting possible influence of flow and flame chemistry. Turbulent scales are biggest for wrinkled and corrugated flamelets.
Damköhler used the geometrical analogy of a flame produced by a Bunsen burner to relate turbulent velocity fluctuations and burning velocity for small scale turbulence. The analogy is best explained using Figure 2.6.

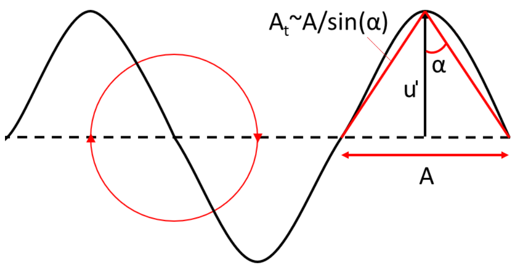

Figure 2.6: Sketch of a turbulent and laminar flame front. The dotted black line shows the laminar flame front. Due to eddies, in the figure depicted with the red circle that rotates clockwise, the flame front gets wrinkled. The sinusoidal shape shows the turbulent flame front.

The flame angle of a Bunsen flame is $sin(\alpha_f) = \frac{S_l}{U_u}$. Figure 2.6 shows that each flamelet could be approached as a Bunsen flame due to the geometrical similarities. The similarities are visualized with the red lines in the flamelet on the right. The flamelet angle, α, is determined from the velocity fluctuation rather than the mean velocity. The velocity fluctuation, u', is depicted with the black arrow. The flamelet angle is $sin(\alpha) = \frac{S_l}{u'}$. Using the analogy between flamelets and a flame produced by a Bunsen burner, the flame surface area and velocity fluctuations are related according to:

$$\frac{A_t}{A} \sim \frac{A/\sin(\alpha)}{A} = \frac{u'}{S_l}. \tag{2.32}$$

Substituting Eq. 2.31 in Eq. 2.32 and for $u' \to 0$, Eq. 2.32 results in:

$$\frac{S_t}{S_l} = 1 + \frac{u'}{S_l}. \tag{2.33}$$

For small scale turbulence, identified in [Peters, 2000] as reaction sheet regime, chemistry plays a significant role in flame-flow interaction and the interaction can no longer be assumed purely kinematic. Damköhler argued that turbulence only modifies transport between reaction zone and unburned gas. The laminar burning velocity scales with the molecular diffusivity, $\mathcal{D}$, and the chemical time scale, τ_{ch}, according to:

$$S_l \sim \left(\frac{\mathcal{D}}{\tau_{ch}}\right)^{\frac{1}{2}}. \tag{2.34}$$

Damköhler proposes to scale the turbulent burning velocity by replacing $\mathcal{D}$ with the turbulent diffusivity, $\mathcal{D}_t$. The ratio of turbulent and laminar burning velocity is then given by:

$$\frac{S_t}{S_l} \sim \left(\frac{\mathcal{D}_t}{\mathcal{D}}\right)^{\frac{1}{2}}. \tag{2.35}$$

The chemical time scale remains unchanged and thus it is assumed that chemical time scale is not affected by turbulence. This assumption does not hold when the Kolmogorov eddies are able to penetrate into the reaction zone which is the case for $Ka_\delta < 1$. $Ka_\delta < 1$ in the broken reaction zone which is why Eq. 2.35 does not hold in the broken reaction zone, see Figure 2.4. Molecular diffusivity is $\mathcal{D}$ proportional to $S_l\delta_f$ and $\mathcal{D}_t$ is proportional to $u'l_0$. Rewriting Eq. 2.35 results in:

$$\frac{S_t}{S_l} \sim \left(\frac{u'}{S_l}\frac{l_0}{\delta_f}\right)^{\frac{1}{2}}. \tag{2.36}$$

For small scale turbulence, turbulent burning velocity is also dependent on the length scale ratio l_0/δ_f.

2.4 Flashback

A premixed flame is stable when the unburned gas velocity is equal to the burning velocity. Increasing gas velocity finally leads to blow off, while decreasing gas velocity leads to flashback. Flashback is the usually undesired upstream flame propagation. In gas turbines, only the combustor is built to withstand high temperatures and flashback would lead to material damage and possibly failure. There are four main flashback mechanisms [Kalantari and McDonell, 2017].

- Core flow flashback: This type of flashback occurs when the burning velocity of the mixture is higher than the velocity in the center of the burner. Core flow flashback can be prevented by increasing the axial velocity.
- Combustion instability induced flashback: Flashback due to combustion instability occurs as a result of large amplitude fluctuations of the flow field.
- Combustion induced vortex breakdown (CIVB): This type of flashback occurs in swirl burners when the flow reverses direction due to vortex breakdown.
- Boundary layer flashback (BLF): This type of flashback occurs when the burning velocity in the boundary layer is higher than the local streamwise velocity. Boundary Layer Flashback is the mechanism studied in this research.

2.4.1 Boundary layer flashback

Lewis and Von Elbe [1943] reported on boundary layer flashback of laminar premixed flames produced by a Bunsen burner. They proposed the critical velocity gradient model. Figure 2.7a shows a schematic of the velocity gradient model. The velocity gradient model was established empirically. In the model it is assumed that axial velocity close to the wall is given by:

$$u(\delta_p) = \frac{\partial u}{\partial y}|_{y=0}\delta_p, \tag{2.37}$$

where δ_p is the wall normal distance to the flame leading tip and is called the penetration distance. The penetration distance should be larger than the quenching distance δ_q because a flame is quenched within quenching distance.

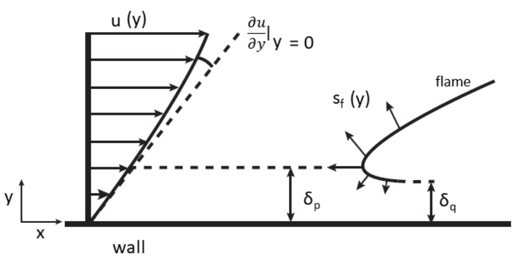

(a) Schematic of velocity gradient model [Faldella, 2019].

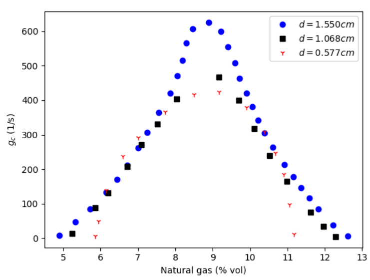

(b) The critical velocity gradient as a function of unburned mixture composition.

Figure 2.7: (a) The curve on the right is the flame leading tip, travelling upstream at wall normal distance $y = \delta_p$. In the model it is assumed that the axial velocity increases linearly with wall normal distance. (b) The critical velocity gradient, g_c, as a function of unburned mixture composition for laminar Bunsen flames with different diameters. Figure 2.7b is reproduced from [Lewis and von Elbe, 1943].

If the velocity, u, is smaller than the laminar flame speed, S_l, flashback will occur. The situation where gas velocity and laminar flame speed are in balance at $y = \delta_p$ is given by:

$$\frac{\partial u}{\partial y}|_{y=0} = \frac{S_l}{\delta_p}, \tag{2.38}$$

where the left hand side of Eq. 2.38 might be described as the flow resistance to boundary layer flashback and the right hand side might be described as the ability of the flame front to travel upstream in the boundary layer. Flashback occurs as soon as the right hand side is larger than the left hand side. The right hand side is called the critical velocity gradient, g_c. The critical velocity gradient is then given by:

$$g_c = \frac{S_L}{\delta_p}. \tag{2.39}$$

Figure 2.7b shows the critical velocity gradient, g_c, as a function of unburned mixture composition for laminar Bunsen flames with different diameters. The values of g_c are determined experimentally.

Figure 2.7b shows that the critical velocity gradient seems to be independent of burner diameter. The velocity gradient model is yet still used to estimate bulk velocity at flashback. The model is able to correlate flashback of laminar flames and in an unconfined set-up also turbulent flames [Putnam and Jensen, 1949] but it does not accurately model flashback in a confined set up because flame-flow interaction can not be neglected in a confined set-up [Eichler and Sattelmayer, 2011].

Effect of turbulence on boundary layer flashback

The critical velocity gradient model was applied to turbulent premixed flames for the first time by [Putnam and Jensen, 1949]. The effect of turbulence on flashback is shown in Figure 2.8.

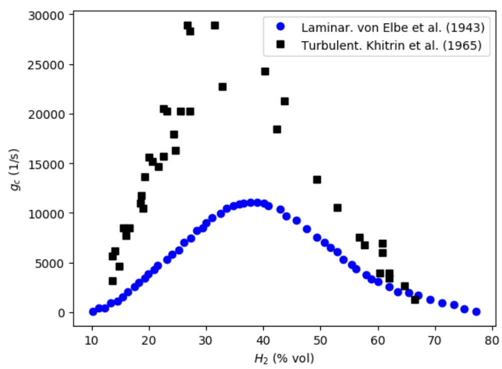

Figure 2.8: Effect of turbulence on the critical velocity gradient. Figure is reproduced from [Kalantari and McDonell, 2017].

Turbulent velocity fluctuations cause the burning velocity to increase. The increased burning velocity in turn increases flashback propensity. For hydrogen-air mixtures a ratio of turbulent and laminar critical velocity gradient $\frac{g_{c,turb}}{g_{c,lam}} \approx 3$ around stochiometric conditions has been observed. The ratio of turbulent and laminar critical velocity gradient seems to hold for other fuels too [Eichler and Sattelmayer, 2011].

Effect of flame confinement on boundary layer flashback

In an unconfined configuration the reactants are freely injected and the flame is not surrounded by a burner wall e.g. a jet flame is an unconfined flame. In a confined set-up

the flame is surrounded by the burner wall and the flame and the wall interact. Eichler and Sattelmayer investigated the effect of flame confinement on the flashback propensity for premixed turbulent hydrogen-air mixtures. It was concluded that the critical velocity gradient model does not hold for confined flames due to flame-flow interaction. Their results show that the local gas velocity is low just upstream of the flame leading tip. Under some conditions, the flow upstream the flame leading tip reverses direction. This phenomenon is called boundary layer separation, and since the flow is locally directed upstream, conditions are perfect for flashback to occur. According to Eichler and Sattelmayer, the combined effect of a flame induced adverse pressure gradient and the presence of low velocity streaks in the turbulent boundary layer cause boundary layer separation [Eichler and Sattelmayer, 2012]. Eichler and Sattelmayer's conclusions were supported by the result of a direct numerical simulation done by Gruber [Gruber et al., 2012].
Eichler and Sattelmayer's results also showed the effect of burner geometry on the flame front location by placing a sharp edge on the lower wall of the duct. The sharp edge functioned as an anchor point.

2.4.2 Flashback prediction models

Hoferichter developed flashback prediction models for premixed unconfined and confined flames. The first section discusses the model predicting flashback of unconfined flames, the second section discusses the model predicting flashback of confined flames.

TU Munich unconfined model

In the present research the model is referred to as TU Munich unconfined model. In the model the laminar unstretched burning velocity, S_l, and the turbulent velocity fluctuations, u', have the largest effect on the bulk velocity at flashback [Hoferichter et al., 2017b].
Hoferichter used Cantera 2.2 with the reaction mechanism of Ó Conaire to obtain values of fluid properties such as the viscosity [ÓConaire et al., 2004]. Free flame simulations at different preheating temperatures were performed to generate a polynomial function of the unstretched laminar burning velocity. The velocity fluctuations are determined with:

$$u'(y_{FB}) = 1.5u_\tau, \tag{2.40}$$

where u_τ is the friction velocity and y_{FB} is the wall distance of flashback initiation. The TU Munich unconfined model uses 'flame angle theory' to relate global and local properties. The global analysis is given by:

$$\sin(\alpha_f) = \frac{\overline{S}_t}{U_{FB}}, \tag{2.41}$$

where α_f is the flame angle, $\overline{S}_t$ is the turbulent burning velocity averaged over the burner area and U_{FB} is the bulk velocity at flashback. The local analysis is given by:

$$\sin(\alpha_f) = \frac{S_t(y_{FB})}{u(y_{FB})}, \tag{2.42}$$

where $S_t(y_{FB})$ is the burning velocity and $u(y_{FB})$ is the axial gas velocity at wall distance y_{FB}. The burning velocities, S_t and $\overline{S}_t$, are modelled with the Damköhler correlation for small scale turbulence. The turbulent burning velocity is discussed is subsection 2.3.1. The full set of equations describing the flashback prediction model is discussed in Appendix A. The underlying assumptions of the model are listed below:

- The Markstein length l_m is only dependent on laminar flame thickness and the Zel'dovich and Lewis numbers.
- Flashback initiates at $y^+ = 16.4$ in the flame front due to a maximum turbulent turbulent velocity fluctuation at that wall distance.

- The Lewis number of the gas mixture is the weighted average of Le_{H2} and Le_{O2} as proposed by Bechtold and Matalon in [Bechtold and Matalon, 2001].
- Flame stretch rate depends only on turbulence and flame front curvature.
- Turbulence is isotropic.

For confined premixed turbulent hydrogen-air flames produced by a channel burner the dimensionless wall normal distance of maximum velocity fluctuation is $y^+ = 16.4$. Experimental results show that for unconfined flames the dimensionless wall normal distance of maximum velocity fluctuation is in the same range as $y^+ = 16.4$ [Baumgartner, 2014].

TU Delft confined model

The model predicting flashback of premixed confined flames uses the Stratford criterion to assess if flow separation occurs. Under the condition of fully developed incompressible flow the Stratford criterion as implemented by Hoferichter reduces to:

$$\sqrt{2}\left(\frac{2\Delta p}{\rho_u U_{FB}^2}\right)^{\frac{3}{2}} = 0.39, \tag{2.43}$$

where Δp is the pressure increase due to the flame induced adverse gradient, ρ_u is the unburned gas density and U_{FB} is the centerline velocity at flashback. The adverse pressure gradient is modelled by:

$$\Delta p = \rho_u S_t^2(\sigma - 1), \tag{2.44}$$

where S_t is the turbulent burning velocity and σ is the ratio of the unburned - and burned gas density.
Tober [Tober, 2019] recommended two modifications to the model for predicting flashback of premixed confined flames. Hoferichter assumed turbulence is isotropic and the first modification was to include the effect of anisotropy of turbulence on flame stretch rate. The second modification is to include the effect of non-unity Lewis number on turbulent burning velocity. The effect of non-unity Lewis number is largest for fuel-lean conditions. In this research, the model predicting flashback of premixed flames in a confined set up including Tober's modifications is referred to as the TU Delft confined model. All assumptions involved in the TU Munich unconfined model are applicable in the TU Delft confined model too, because both models determine the turbulent burning velocity, S_t, with the Damköhler correlation for small scale turbulence.

3 Methodology

3.1 Experimental set-up

Figure 3.1 shows a schematic view of the experimental set-up. The set-up is the same as previously used by [Faldella, 2019].

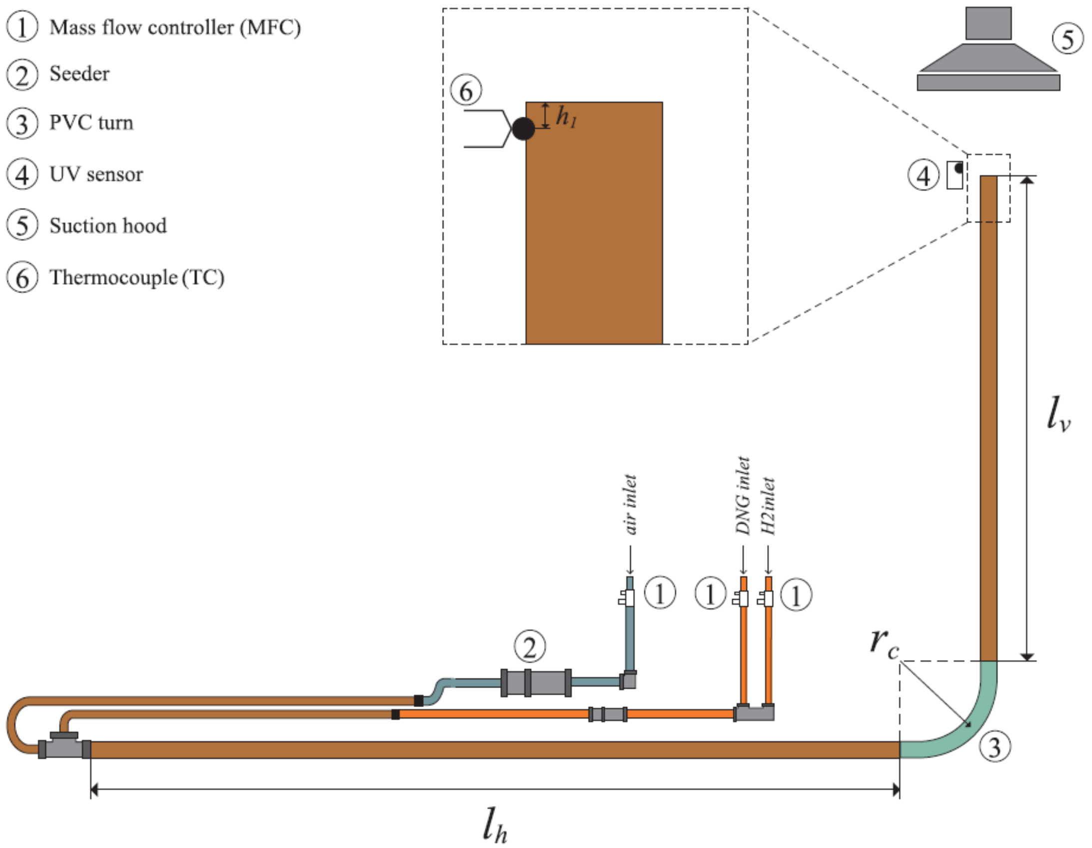

Figure 3.1: Schematic view of the burner set-up used in the present research. The schematic was first reported in [Faldella, 2019].

Three mass flow controllers were used to control gas inlet lines of hydrogen, DNG and air. All mass flow controllers are manufactured by Bronkhorst. The uncertainty is 0.1% from the full scale and 0.5% for the reading of the flow rate. The valves upstream the mass flow controllers ensure that gas at the mass flow controller inlet is at suitable pressure which is 5 bar ± 2% for the H_2 and air mass flow controllers and 2 bar ± 2% for the DNG mass flow controller. The UV-sensor depicted in Figure 3.1 shuts down the fuel supply if the flame is not 'visible' to the sensor. The thermocouple was placed at $h_1 = 4$ mm upstream the burner rim on the outside of the burner wall.

Experiments were done with copper tubes of two different diameters. To ensure fully developed turbulent pipe flow a high length-over-diameter ratio, l/d, is required. It is not possible to reach this ratio with one straight pipe because the height of the lab is limited.

Fully developed turbulent pipe flow was achieved with a 90° bend [Faldella, 2019]. The 90° bend, part 3 in Figure 3.1, makes it possible to increase pipe length within the lab. See Table 3.1 for the details on the experimental set-up.

Tube 1	**Vertical tube**	**Horizontal tube**	**Turn**
$d_{internal}$ (mm)	19.76 ± 0.04	20.06 ± 0.04	
Thickness (mm)	1	1	
Length (mm)	1250	1450	
$\frac{l}{d}$ (-)	63.26	73.38	
$r_{curvature}$ (mm)			85
Material	copper	copper	PVC
Tube 2	**Vertical tube**	**Horizontal tube**	**Turn**
$d_{internal}$ (mm)	25.20 ± 0.04	25.67 ± 0.04	
Thickness (mm)	1.1	1.1	
Length (mm)	1250	2400	
$\frac{l}{d}$ (-)	49.60	95.24	
$r_{curvature}$ (mm)			88
Material	copper	copper	PVC

Table 3.1: Details of the experimental set-up.

The mass flow controllers communicate with Labview. The parameters in the mass flow controllers were set such that these respond quickly without a large overshoot. The flow is measured in normal liters per minute, in Eq. 3.1 denoted with $Q_{reading}$. The actual flow rate is given by:

$$Q_{actual} = Q_{reading} \left(\frac{p_n}{p}\right) \left(\frac{T}{T_n}\right), \tag{3.1}$$

where Q_{actual} is the actual flow rate in liters per minute and T_n and p_n are the reference temperature and pressure, respectively. The reference temperature and pressure are $T_n = 0°C$ and $p_n = 0$ bar. Note that Eq. 3.1 is valid under the assumption that the gas going through the mass flow controllers behaves as an ideal gas. The pressure, p, and temperature, T, in the lab were measured continuously and fed as input in the mass flow controllers using Labview. Table 3.2 lists all input and output parameters relevant to the experiments. It is also listed how the parameters were measured during the experiment.

	Input	**Output**
percentage H_2	Volumetric balance equations in labview back panel	MFC
equivalence ratio	Stochiometric equations in labview backpanel	MFC
Bulk velocity	$\frac{\dot{Q}}{A_{burner}}$ in backpanel labview	MFC
Temperature	Labview	Thermocouple and weather station
Pressure	Labview	weather station
Diameter	Labview	three point inner micrometer
BL obstruction	Manually, by rotating a screw	-

Table 3.2: Flashback map parameters

In the Labview frontpanel input conditions are set. In the Labview backpanel the input values are translated into input for the mass flow controllers through balance equations. The mass flow controller output is continuously displayed in the Labview frontpanel. So with the frontpanel it is possible to verify whether the calculated, or set, output parameters match with the true output. See Appendix G1 for the frontpanel and Appendix G2

for the governing balance equations in the backpanel.
Cooling jackets were used to control burner wall temperature, see Figure 3.2. Some experiments were done without cooling jackets to investigate the effect of the wall temperature. The performance of the cooling jackets was tested with one K-type thermocouple 4 mm upstream the burner exit. During all tests, a temperature below 60° C was maintained.

3.1.1 Boundary layer obstruction

A screw acting as a cylindrical obstacle was placed in the boundary layer, see Figure 3.2.

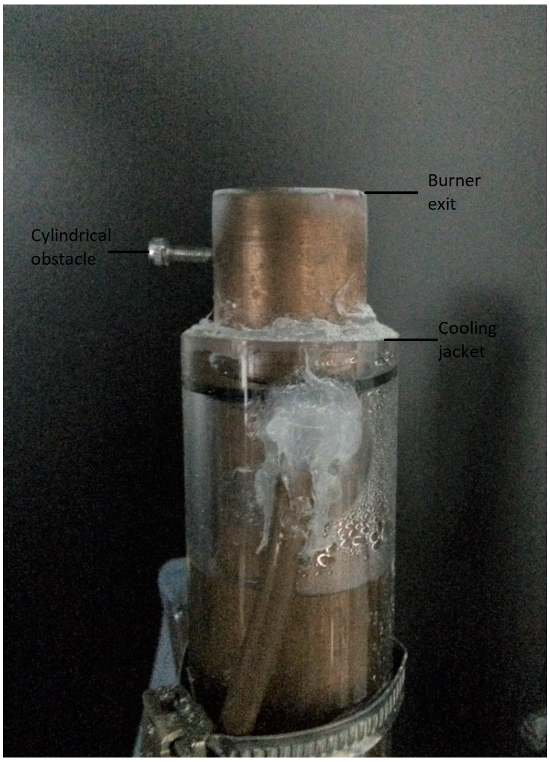

Figure 3.2: The Bunsen burner with screw placed 10 mm upstream the burner exit. The cooling jacket is the PVC component with the rim placed ≈ 20 mm downstream the burner exit.

A hole with M3 screw thread was made 10 mm upstream of the burner exit. By rotating the screw, the obstruction height in the boundary layer was varied. Normal conditions were reached by adjusting the screw such that the screw tip was flush with the burner inner wall. Each clockwise rotation adds 0.5 mm to the obstruction height. The average inner and outer diameter of a M3 screw are 2.35 mm and 2.927 mm, respectively. The average screw diameter is the average of the sum of the inner and outer diameter and is 2.641 mm. With every clockwise rotation the BL obstruction area increases thus with $2.641 * 0.5 = 1.321$ mm^2.

3.2 Planar Partice Image Velocimetry

3.2.1 Tracer particles

Particle Image Velocimetry (PIV) was used to obtain velocity data in a planar cross section of the flow in a non-intrusive manner. A drawback of two-component PIV-measurements is that the out-of-plane velocity component can not be measured [Faldella, 2019].
Alumina particles with an average diameter of 1 µm and a density of $\rho_p = 3200$ kg/m^3 were seeded in the air flow far upstream of the burner exit. Downstream the seeder, fuel and

air were mixed. The seeding material is chosen such that it does not alter flame chemistry when used in amounts suitable for PIV. The particle inertia defines how well the particles respond to variations in gas velocity. If particle inertia is too high the particle streamlines will not describe the flow. According to Tropea [Tropea, 2007] a particle behaves like a tracer particle if the Stokes number is much smaller than 0.1. The condition is given by:

$$Stk = t_0 \frac{u_0}{l_0} << 0.1, \tag{3.2}$$

where u_0 and l_0 are velocity and length scales typical for the flow. In order to trace the smallest eddies, Eq. 3.2 should hold for $u_0 = u_\eta$ and $l_0 = \eta$, where u_η and η are the Kolmogorov velocity and length scales, respectively, see subsection 2.2.4.
Somerscales proposes the following simplified equation of motion of a particle moving in a viscous fluid [Somerscales, 1981]:

$$\rho_p \frac{d_p^3}{6} \frac{du_p}{dt} = 3\mu_f d_p (u_f - u_p), \tag{3.3}$$

where ρ_p is the particle density, d_p is the particle diameter, u_p and u_f are the particle and fluid velocity, respectively, and μ_f is the fluid dynamic viscosity. The left hand side of Eq. 3.3 represents particle acceleration and the right hand side represents viscous drag of flow. Eq. 3.3 holds under the following five assumptions [Faldella, 2019] [Tropea, 2007]:

- The particle Reynolds number is smaller than one, $Re_p = \frac{(u_p - u_f) d_p}{\nu_f} < 1$.
- The flow is incompressible and of infinite extend.
- The particles are rigid and spherical.
- The no slip condition holds at the particle surface.
- $\rho_p >> \rho_f$.

Using Eq. 3.3, an expression for t_0 in Eq. 3.2 might be found. Integrating Eq. 3.3 with respect to time, t, gives:

$$u_p = u_f e^{-\frac{18\mu_f}{\rho_p d_p^2} t} = u_f e^{-\frac{t}{t_0}}, \tag{3.4}$$

where $t_0 = \frac{\rho_p d_p^2}{18\mu_f}$ is the particle relaxation time. The particle relaxation time might be substituted for the time scale t_0 in Eq. 3.2. The smaller the relaxation time, the faster the particles adept to flow fluctuations and the better the flow characteristics are captured with PIV measurements. The Stokes number was calculated for the smallest eddies under the assumption that the logarithmic sublayer exists. With a maximum axial velocity fluctuation of 3.5 m/s reported in this research, the Stokes number is 0.00041 << 0.1 so that the particles behave like tracer particles under the assumptions mentioned above and under the energy cascade assumption.

3.2.2 PIV equipment

Most information in this section is extracted from Faldella's work [Faldella, 2019]. The measuring tools consist of a laser, a camera, a PIV seeder, a controller and a computer. The laser set up is shown in Figure 3.3.

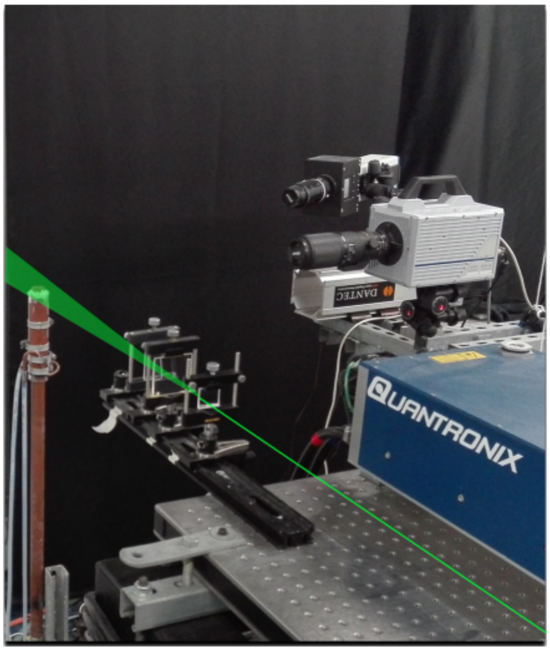

Figure 3.3: The PIV set-up with the laser, the lightsheet optics and the camera. The tube burner is visible on the left [Faldella, 2019].

The laser emits green light with a wavelength of 527 nm. Three plano-concave cylindrical lenses transform the laser beam into a sheet. The laser beam is produced by a QuantronixNd:YLF dual-cavity laser type Darwin-Duo Pro527-80-M.
A Phroton Fastcam SA1.1 camera was used to make pictures. The maximum sensor size is 1024x1024 pixels. The maximum frame rate using the whole sensor is around 3 kHz in double frame mode. Some experiments required a higher frame rate, which is why the sensor was sometimes cropped. The camera central axis was set normal to the laser sheet. The lens used is a Nikon AF Micro-NIKKOR 200 mm f/4D IF-ED lens.
The screw is placed parallel to and in the laser sheet. A programmable timing unit (PTU) was used to synchronize laser pulses and camera shutter. Davis 8.4.0 was used to control the PTU, to record experiments and to process data.
In single frame mode, the time between to laser pulses is the inverse of the frame acquisition rate, given by:

$$\Delta t = \frac{1}{f}, \tag{3.5}$$

where Δt is the time between pulses in single frame mode and f is pulse frequency. The lower limit of the pulse frequency is 50 Hz. The time between pulses was optimized by trial and error. A rule of thumb is that the correlation is optimal if the seeding particles travel a quarter of the interrogation area size between two sequential laser pulses. In double frame mode the time between pulse 1 and 2 can be set.

3.3 Flashback map

The goal of the experiment described in this section is to get insight in the effect of the obstruction height on the bulk velocity at flashback, U_{FB}. All experiments were repeated at least twice. First, a flashback map for zero obstruction height was determined and compared to the map reported by [Faldella, 2019] to check the reproducibility of the experiment. Then, the effect of the obstruction height on the bulk velocity at flashback was investigated for different hydrogen/DNG/air mixtures and for fuel-lean and fuel-rich conditions.

3.4 Coldflow

In all non-reacting pipe flow experiments the lowest frame rate possible with this system was used. The data sets obtained each contain 3563 images to decrease statistical scatter. The non-reacting flow was recorded for three different settings, see Table 3.3.

h_{obstr} (mm)	**0**	**1**	**2**
$\mathrm{Re_D}$ (-)	10000 ±10	10000 ±10	10000 ±10
Gas composition	air	air	air
Temperature (° C)	22 ± 1	22 ± 1	22 ± 1
Pressure	ambient	ambient	ambient
Frame rate (Hz)	50	50	50
Δt (ms)	50	50	50
n_{frames} (-)	3563	3563	3563
Time (s)	71	71	71
Sensor size (pixels)	896x896	896x896	896x896

Table 3.3: Experimental settings for the non-reacting pipe flow. All experiments were done in double frame mode. Davis 8.4.0 was used to control the measure equipment and to process the data. The number of frames is n_{frames}.

To obtain a vector field the system operated in double frame mode. The raw data was processed in Davis 8.4.0. The first processing step was cross-correlation with multiple passes. The first interrogation area size was 48x48 pixels with two passes, the second 16x16 pixels with three passes and 50% overlap. Correlation is optimal if particles travel around a quarter of the interrogation area and if the seeding density is between 8 and 10 particles per interrogation area. The missing vectors were interpolated. The resulting vector field was accepted if the first and second choice vectors together form at least 95% of all vectors. Universal Outlier detection was used to validate each vector. The validity of the results obtained through Davis was tested by integrating the velocity profile with respect to the burner diameter as to determine the bulk velocity:

$$U_{bulk} = \frac{2\pi \int_0^{d_i/2} \overline{u}(r) r dr}{\pi d_i^2/4}. \tag{3.6}$$

The bulk velocity obtained through integration of the mean velocity profile deviates by 7% from the bulk velocity as determined from the mass flow meter. Other than to construct a mean velocity profile the data obtained in the present research was used to determine the Reynolds stresses.

3.5 Reacting field

This section consists of three subsections. Four method to determine flame front location are discussed in section 3.5.1. The experiment discussed in section 3.5.2 focuses on a stable flame. The goal of the experiment to get insight in the relation between turbulent velocity fluctuations, u', low velocity streaks and bulk velocity at flashback, U_{FB}. The experiment discussed in subsection 3.5.3 focuses on the flashback process. Flashback of a flame produced by a burner with smooth walls was qualitatively compared to flashback of a flame produced by a burner with an obstruction in the flow. The goal of the experiment is to get insight in the relation between boundary layer obstruction and flame front location.

3.5.1 Flame front location

To determine flame front location four methods were compared. The underlying assumption of each method is listed below.

- Method 1: The underlying assumption of method 1 is that the radial coordinate of the flame front location at a particular axial station corresponds to the location where the intensity values of raw images of the PIV seeding particles equal the average value of the intensity values in burned and unburned gas regions. This method was also used by [Faldella, 2019].
- Method 2: The instantaneous flame front is not stationary, resulting in large variations in intensity in the vicinity of the time-averaged flame front location because the seeding density in the unburned gas is higher than the seeding density in the burned gas due to expansion. The underlying assumption of method 2 is that the flame front location at a particular axial station corresponds to the location of the peak in RMS value of the intensity of the raw PIV images at that axial station.
- Method 3: The instantaneous flame front is not stationary, resulting in large instantaneous velocity differences in and around the time-averaged flame front location. The underlying assumption of method 3 is that the flame front location at a particular axial station corresponds to the location of the peak in RMS value of the velocity field at that axial station.
- Method 4: The underlying assumption of method 4 is that the flame front location at a particular axial station corresponds to the radial coordinate where the reacting flow field characteristics (mean velocity and Reynolds stresses) start to deviate qualitatively from the non-reacting flow field characteristics.

After comparing the methods it was concluded to use method 3 to determine flame front location and flame angle because the method is the least susceptible to human error and for the case with zero obstruction height the flame front is the most axisymmetric when determined with method 3. For the comparison of method 1 and 3 see section 4.3.1 and for more details on method 1, 2 and 4 see Appendix C.
The underlying assumption of method 3 is that the flame front location at a particular axial station corresponds to the location of the peak in root mean square of the velocity field at that axial station. The root mean square of the velocity field is given by:

$$U_{RMS} = \sqrt{\frac{1}{2}(\overline{u'^2} + \overline{v'^2})}, \tag{3.7}$$

where U in U_{RMS} does not imply 'axial'. Figure 3.4a shows the root mean square of the velocity field for the case 60% H_2 and $h_{obstr} = 0$ mm. The flame front location as determined by method 3 is shown in Figure 3.4b for four different values of the obstruction height, h_{obstr}.

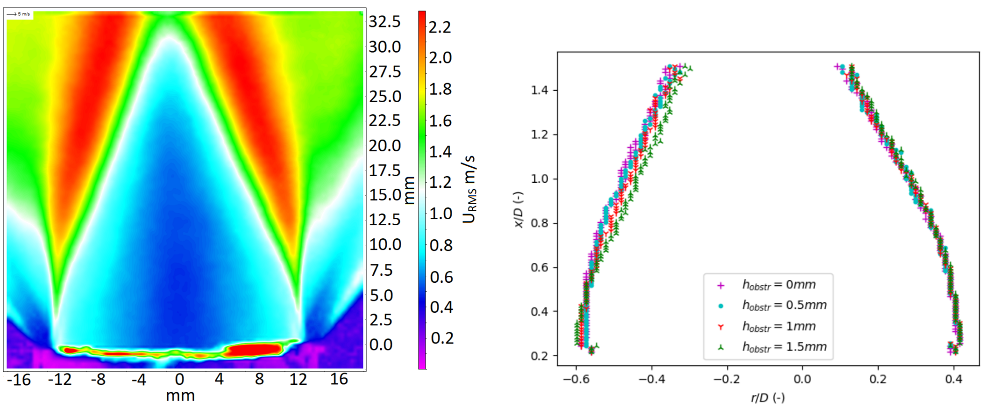

(a) u_{RMS} of a flame on a Bunsen burner with smooth walls.

(b) Flame front location determined by method 3 for four values of the obstruction height.

Figure 3.4: The figures are shown for the 60%H_2 case. The experimental conditions were Re_D = 10500, d_i = 25.20 mm, U_{bulk} = 7.1 m/s and ϕ = 1.

Figure 3.4b shows that the flame front locations for the different values of h_{obstr} overlap for $r > 0$. However, for $r < 0$ the flame front radial coordinate at a particular axial station decreases with increasing obstruction height h_{obstr}.

3.5.2 Stable flame

The gas mixtures studied in this particular experiment contain 60%, 80%, and 100% H_2. For each gas mixture the obstruction height was varied while keeping all other parameters constant. To ensure all other parameters stayed constant the Reynolds number was chosen such that the gas velocity was set at approximately 0.5 m/s above the bulk velocity at flashback for the case $h_{obstr} = 1.5$ mm. Table 3.4 lists all parameters per gas mixture. The PIV system operated in double frame mode.

Fuel composition %H_2	60	80	100
$\mathrm{Re_D}$ (-)	10500 ±10	15800 ±10	23400 ±10
Bulk velocity (m/s)	7.1	11.4	19.1
h_{obstr} (mm)	0-1.5	0-1.5	0-1.5
Wall T (° C)	< 60	< 60	< 60
Pressure (bar)	ambient	ambient	ambient
Frame rate (kHz)	150	200	400
Δt (ms)	40	25	16
n_{frames} (-)	2683	2113	2394
Time* (s)	60	60	60
Sensor size (pixels)	896x896	896x896	896x896
Diameter (mm)	25.20	25.20	25.20
Equivalence ratio (-)	1	1	1
Kinematic viscosity (m$^2/s$)	1.68e-5	1.80e-5	2.06e-5

*Table 3.4: The experimental settings for the cases 60, 80 and 100 % H_2. The number of frames is n_{frames}. * The total time cannot be calculated with the total number of frames because sometimes only the first and last part of a recording were used to increase measuring time.*

The data obtained contains at least 2000 image pairs per data set and was taken over at least one minute. The sensor size was cropped to 896x896 pixels to increase the maximum number of frames in the camera RAM. Also, the pulse frequency was increased compared to the frequency used during the non-reaction pipe flow experiments to decrease shutter time. Too large shutter time increases noise due to flame luminosity. The raw PIV images were processed in Davis 8.4.0. The first processing step was cross-correlation with multiple passes. The first interrogation area size was 48x48 pixels with two passes, and the second 16x16 pixels with three passes and 50% overlap. The resulting vector field was accepted if the first and second choice vectors together formed at least 95% of all vectors. Universal Outlier detection was used to validate each vector.

3.5.3 Flashback process

After the burner produced a stable flame the gas velocity was decreased slowly by decreasing the flow rate, finally leading to flashback. A stable flame was created with the settings as listed in Table 3.5. Every experiment in Table 3.5 was done three times. Faldella's results [Faldella, 2019] suggest that a typical flashback time for the case 100% H_2 is $t_{FB} \sim 1$ ms. To ensure that flashback is at least captured in a sequence of ten consecutive images, the minimum sampling frequency used is 10 kHz. The laser operated in single frame mode.

Gas mixture ($\%H_2$)	0	40	50	100
$\mathrm{Re_D}$ (-)	1300 ±10	4000 ±10	5750 ±10	14000 ± 10
U_{bulk} (m/s)	1.1	3.9	4.7	13.8
h_{obstr} (mm)	0-1	0-1	0-1	0-0.5
Wall T (° C)	< 60	< 60	< 60	< 60
Pressure (bar)	ambient	ambient	ambient	ambient
Frame rate (kHz)	10	10	12	16
Δt (ms)	0.100	0.100	0.083	0.063
n_{frames} (-)	500	500	500	500
Time* (ms)	7.0	4.0	3.0	1.5
Sensor size (pixels)	896x896	896x896	896x896	896x896
Diameter (mm)	19.76	19.76	19.76	19.76
ϕ (-)	1	1	1	1
ν (m^2/s)	1.43e-5	1.56e-5	1.62e-5	2.06e-5

*Table 3.5: The experimental settings for the cases 0, 40, 50 and 100 % H_2. The total number of frames is n_{frames}. *The flashback time and the number of frames are not directly related because some of the frames captured the steady process before flashback occurred.*

4 Results and Discussion

4.1 Flashback map

Flashback maps give insight in the stable operating regime of a certain burner. In a flashback map the bulk velocity at flashback, U_{FB}, is plotted on the vertical axis and equivalence ratio, ϕ, on the horizontal axis for different gas mixtures. The relation between U_{FB} and ϕ is plotted for different fuel/air mixtures. An example of a flashback map is given in Figure 4.1. Figure 4.1 is compared to the results of Faldella [Faldella, 2019] in Appendix D.

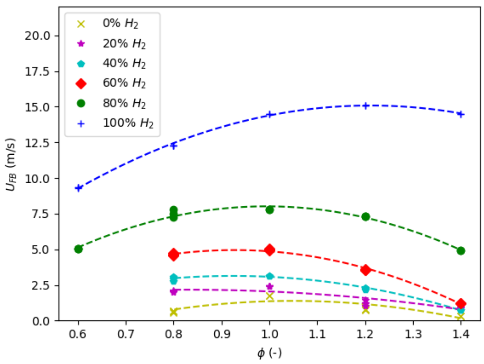

Figure 4.1: Example of a flashback map for hydrogen/DNG/air mixtures as determined in a Bunsen burner with 19.76 mm inner diameter and a cooled tip.

The bulk velocity at flashback, U_{FB}, as a function of equivalence ratio, ϕ, is shown for hydrogen/DNG/air mixtures with fuel mixtures containing 0%, 20%, 40%, 60%, 80% and 100% H_2. Each experiment is done twice, unless mentioned otherwise. The results of each individual experiment is shown in Figure 4.1. However, the scatter is small and some data points completely overlap which is why it seems some measurements are done only once.
The dashed line is a second order fit based on the average value of each experiment. The flame is stable against flashback when $U_{bulk} > U_{FB}$. This condition is satisfied in the area above a curve. For example: for a 20% H_2 hydrogen/DNG/air mixture the stable operating regime is the area above the 20% H_2 curve. Note that blow off is not taken into account in Figure 4.1. Measurements for 0, 20, 40 and 60% H_2 at $\phi = 0.6$ are missing. It was not possible to create a stable flame under these conditions.
The flashback map was constructed as follows. First, a stable flame was created by choosing ϕ and U_{bulk} such that $U_{FB} < U_{bulk} < U_{blowoff}$. Then, the bulk velocity was reduced in small steps till flashback occurs. Steps are typically of the order ~ 0.1 m/s. Before reducing the bulk velocity, the measured hydrogen, DNG and air flow rates were compared to the set flow rates to ensure that the real equivalence ratio and gas composition are as set. Each experiment was repeated once before changing equivalence ratio or gas composition.
The 0% H_2 curve peak is located at $\phi \simeq 1.05$. Burning velocities are highest when adi-

abatic flame temperature is highest, and for hydrocarbon gas mixtures the maximum adiabatic flame temperature is reached when $\phi \simeq 1.05$ because then CO_2 dissociates into CO dropping the mixture specific heat [Faldella, 2019]. The 80% H_2 curve peak is located at $\phi \simeq 1.0$ and the 20%, 40% and 60% H_2 curve peaks are located at $\phi \simeq 0.9$. For 100% H_2 the peak is shifted to fuel-rich conditions because of the fuel-rich stochiometry of the first step in the H_2 reaction mechanism [Sánchez and Williams, 2014]. The first step in the H_2 reaction mechanism is given by:

$$3H_2 + O_2 \rightleftharpoons 2H_2O + 2H. \tag{4.1}$$

Eq. 4.1 shows that the equivalence ratio of the reactants is $\phi = 1.5$. The fuel-rich stochiometry of the first step in the H_2 reaction mechanism and the high contribution from H_2 to the thermal diffusivity shift the curve peak to an equivalence ratio of $\phi \simeq 1.7$.

4.1.1 The boundary layer obstruction

Figure 4.2 compares the flashback map of a Bunsen burner with smooth walls ($h_{obstr} = 0$ mm) to that for a cylindrical obstacle of height $h_{obstr} = 1.5$ mm placed on the inner surface of the tube. The obstruction height is the distance from burner wall to obstacle tip.

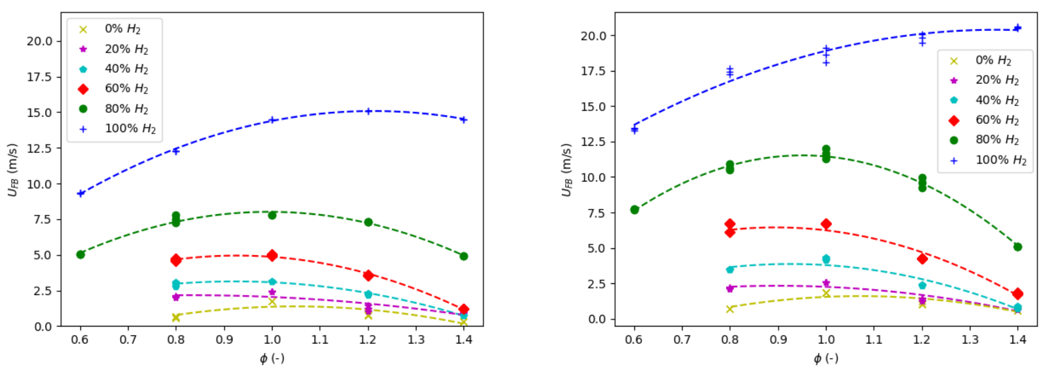

(a) h_{obstr} = 0 mm. *(b) $h_{obstr} = 1.5$ mm.*

Figure 4.2: Effect of the boundary layer obstruction on the flashback propensity. Both flashback maps were produced using a Bunsen burner with 19.76 mm inner diameter and a cooled tip. Figure 4.2a is the reference case and is identical to Figure 4.1.

The quantitative difference in U_{FB} in the figures shows that obstruction height, h_{obstr}, strongly influences flashback propensity. The peak location of both data sets are similar so the boundary layer obstruction has no effect on the peak location.
Figure 4.3 shows the bulk velocity at flashback, U_{FB}, as a function of the dimensionless obstruction height, h_{obstr}/D for the cases 60, 80 and 100% H_2 because those cases are studied in the reacting field experiments. Note that not ϕ but h_{obstr} is on the horizontal axis. This implicitly means that equivalence ratio was kept constant.

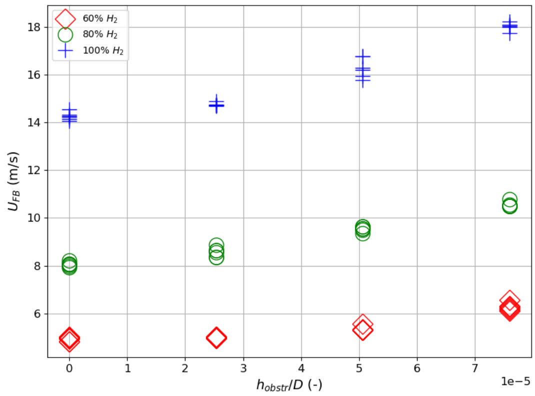

Figure 4.3: The bulk velocity at flashback, U_{FB}, as a function of the dimensionless obstruction height, h_{obstr}/D, for the cases 60, 80 and 100% H_2 for $\phi = 1$ produced using a Bunsen burner with 25.20 mm inner diameter. The measurements were repeated five times.

Figure 4.3 does not show a clear relation between obstruction height, h_{obstr}, and gas composition because the obstruction height seems to have the most effect for the case 80% H_2 and the least for the case 60% H_2. The bulk velocity at flashback increases with obstruction height for all gas mixtures. All experiments in Figure 4.3 were done five times.

4.2 Coldflow

Cold flow experiments were carried out to determine whether the flow issuing from the tube can be considered as fully developed, turbulent pipe flow. To this end PIV measurements were taken in a near field of a tube burner for $Re_D = 10000$ and velocity statistics were extracted at $x = 0.186D$ downstream the burner exit. The velocity statistics were then compared to the results of LDA measurements in the near field of a jet located at $x = 0.186D$ and at $Re_D = 23000$ [Tummers et al., 2011]. Figure 4.4 shows the mean velocity profile, the Reynolds normal stresses in axial and radial direction and the Reynolds shear stress for measurements reported by Tummers et al. and for the present experiments for three cases; i.e. $h_{obstr} = 0, 1$ and 2 mm.

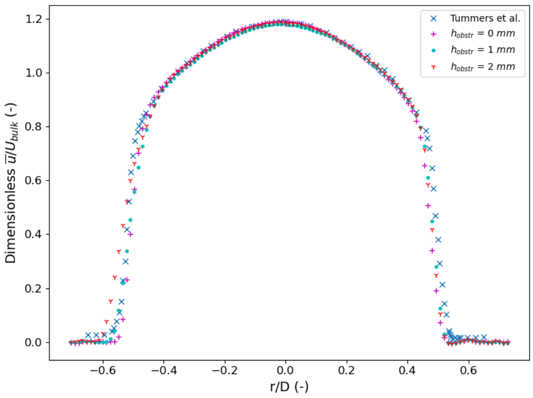

(a) Dimensionless mean velocity component for the axial direction.

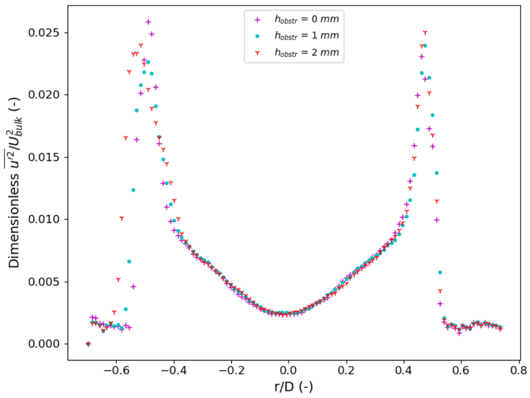

(b) Dimensionless Reynolds normal stress for the axial direction.

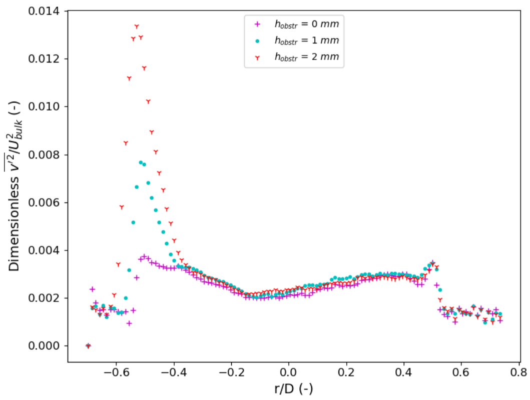

(c) Dimensionless Reynolds normal stress for the radial direction.

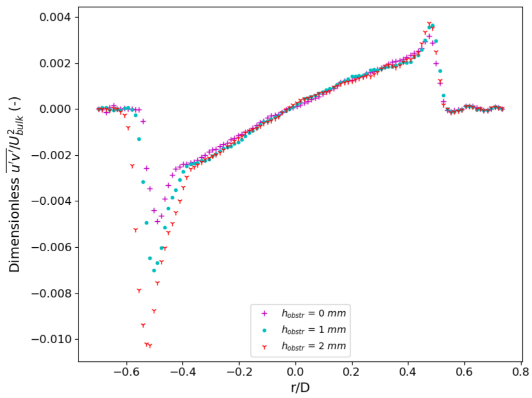

(d) Dimensionless Reynolds shear stress.

Figure 4.4: Flow characteristics of non-reacting flow at a dimensionless distance of x/D = 0.186 downstream the burner exit. The tube inner diameter is d = 25.20 mm, and the experiments conducted at a Reynolds number of Re_D = 10000. The Reynolds stresses were normalized with the bulk velocity. The bulk velocity is 6.17 m/s. Tummers' LDA measurements were conducted at Re_D = 23000.

It is seen in Figure 4.4a that the mean velocity profile corresponds well with Tummers' data and hence the flow is considered turbulent and fully developed. The effect of the obstruction can be observed at the left hand side, near r/D = -0.5. For $-0.5 \leq r/D \leq -0.4$, the mean velocity appears to decrease with increasing obstruction height. However, for $-0.6 \leq r/D < -0.5$, the mean velocity appears to increase with increasing obstruction height. The increased mean velocity observation is supported by the locally increased Reynolds shear stress, see Figure 4.4d. The mean velocity profile visualized in Figure 4.4a was integrated with respect to the radius r to compare the outcome with the bulk velocity computed as $\dot{V}/A$. The integrated mean velocity profile resulted in $U_{bulk} = 5.75$ m/s. The bulk velocity computed as $\dot{V}/A$ is $U_{bulk} = 6.17$ m/s. The bulk velocity found by integrating differs 7% from the bulk velocity computed as $\dot{V}/A$.

Figure 4.4b shows the dimensionless Reynolds normal stress profile in axial direction for the cases $h_{obstr} = 0, 1$ and 2 mm. It is seen in Figure 4.4b that the data sets only deviate for $r/D \leq -0.35$, showing that the boundary layer obstruction only influences the flow downstream the obstruction. The maximum Reynolds normal stresses in axial direction are within 10% deviation when compared to each other. The curve peak of the case $h_{obstr} = 2$ mm is on the left hand side of the curve peak of $h_{obstr} = 0$ mm. The curve peak of $h_{obstr} = 1$ mm is also slightly shifted to the left.

Figure 4.4c shows the profile of the Reynolds normal stress for the radial direction. The peak location of the Reynolds normal stress in radial direction for the case $h_{obstr} = 2$ mm

is slightly shifted to the left when compared to the $h_{obstr} = 0$ mm case. For $r \leq -0.35$ the Reynolds axial stress increases strongly with increasing screw tip height.
Figure 4.4d shows the Reynolds shear stress profile. For $r/D \leq -0.35$ the shear stress increases with increasing screw tip height. The results shown in this figure correspond to the results in Figure 4.4a, where the locally increased velocity indicates increased shear.
Hoferichter found a peak in the velocity fluctuations profile at a dimensionless wall normal distance $y^+ = 16.4$. Hoferichters results are supported by Baumgartners experimental results [Baumgartner et al., 2016] and by Grubers direct numerical simulation [Gruber et al., 2012]. An expression for y^+ is given by:

$$y^+ = \frac{yu_\tau}{\nu}, \tag{4.2}$$

where u_τ is the shear velocity. The shear velocity for non-reacting pipe flow is determined by:

$$u_\tau^2 = 0.03955 U_{FB}^{7/4} \nu_u^{1/4} d^{-1/4}, \tag{4.3}$$

where U_{FB} is the bulk velocity at flashback, ν_u is the kinematic viscosity of the unburned gas and d is the diameter. The velocity fluctuations as presented in this research peak at the same wall normal distance for the case $h_{obstr} = 0$ mm.

4.3 Reacting field

4.3.1 Flame front location

Four methods to determine the flame front location were evaluated. The methods are discussed in more detail in Section 3.5.1 and the flame fronts determined by the methods are included in Appendix C. The underlying assumption of each method is listed below.

- Method 1: The underlying assumption of method 1 is that the radial coordinate of the flame front location at a particular axial station corresponds to the location where the intensity values of raw images of the PIV seeding particles equal the average value of the intensity values in burned and unburned gas regions, corresponding to [Faldella, 2019].

- Method 2: The underlying assumption of method 2 is that the flame front location at a particular axial station corresponds to the location of the peak in RMS of the intensity of the raw PIV images at that axial station.

- Method 3: The underlying assumption of method 3 is that the flame front location at a particular axial station corresponds to the location of the peak in RMS of the velocity field at that axial station.

- Method 4: The underlying assumption of method 4 is that the flame front location at a particular axial station corresponds to the radial coordinate where the reacting flow field characteristics (mean velocity and Reynolds stresses) start to deviate qualitatively from the non-reacting flow field characteristics.

Method 4 is most susceptible to human error compared to the other methods. For $x/d \geq 0.7$, method 2 models the flame front too close to the central axis because root mean square of the intensity is highest at the central axis for $x/d \geq 0.7$. The flame front for the case 60% H_2 and $h_{obstr} = 0$ mm determined by method 1 and method 3 are compared in Figure 4.5.

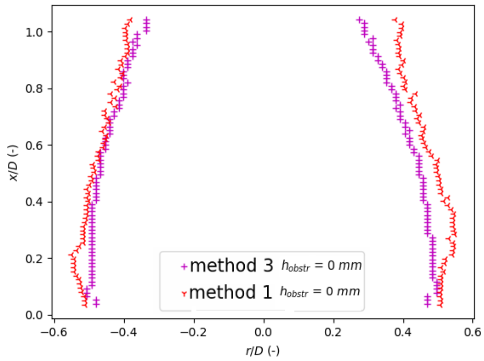

Figure 4.5: Flame front location determined by method 3 and 1 for the case 60% H_2 and $\phi = 1$ with smooth burner walls, $h_{obstr} = 0$ mm.

Due to the flame induced pressure gradient the unburned gas is bended outward over the burner rim and the flame extends beyond the burner rim. This process is observed for unconfined flames and is called flame overhang. Flame overhang seems to be captured by method 1 and not by method 3. However, the flame front determined with method 3 is more axisymmetric than the flame front determined with method 1. For $x/d > 0.8$ the flame front determined with method 1 diverges. This is a result of a too small camera field of view. Hence, method 3 is used in this research to determine flame front location and flame angle.

4.3.2 Velocity fluctuations and flame angle

The quantity x_{FF} is defined as the axial coordinate of the flame front at radial position $y^+ = 16.4$. The value of x_{FF} was found using the flame front modelled with method 3. Figure 4.6 shows how the downsteam locations were found. The axial location, x_{FF}, of the flame front plotted in Figure 4.6 is $x_{FF} = 0.4d$.

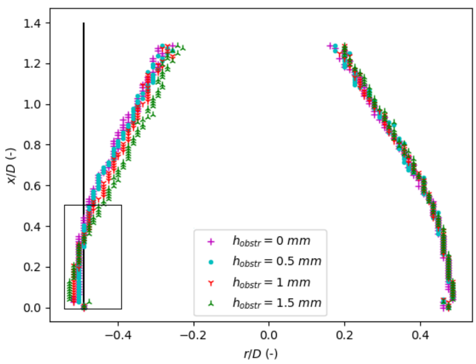

(a) Flame front determined with method 3 for different values of the obstruction height.

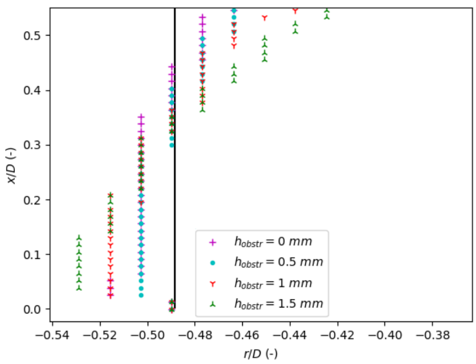

(b) Zoom of Figure 4.6a.

Figure 4.6: The solid black line corresponds to the line $y^+ = 16.4$. The solid black rectangle in Figure 4.6a marks the boundaries of Figure 4.6b. The solid black line is plotted for a mixture containing 60% H_2 and for $h_{obstr} = 0$ mm. The flame was produced by a tube burner with $d = 25.20$ mm and for $\phi = 1$. The bulk velocity was U_{bulk} = 7.1 m/s corresponding to Re = 10500.

The flame front location, x_{FF}, was found by interpolating between two intervals. The wall normal distance of flashback initiation, y_{FB}, is given by Eq. 4.2. The wall normal

distance of flashback initiation is dependent on bulk velocity at flashback, U_{FB}, and kinematic viscosity, ν_u. Hence, the wall normal distance of flashback initiation is dependent on obstruction height and gas composition which is why figures similar to Figure 4.6 were made for every setting in Table 4.1.
Turbulent velocity fluctuations in the flame front at radial position $y^+ = 16.4$ and axial position x_{FF} were determined for different obstruction heights, h_{obstr}, for the cases 60, 80 and 100% H_2. Figure 4.7 shows axial and radial velocity fluctuations at a fixed downstream location x_{FF} on the left hand side and right hand side, respectively.

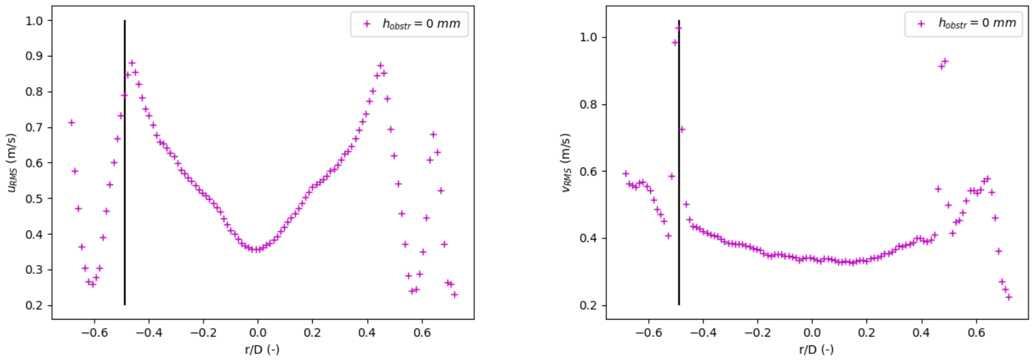

(a) u_{RMS}. *(b) v_{RMS}.*

Figure 4.7: Velocity fluctuations u_{RMS} and v_{RMS} at fixed downstream position $x = x_{FF}$. The solid black line corresponds to the line $y^+ = 16.4$. The flame was produced by a tube burner with inner diameter $d = 25.20$ mm for the case 60% H_2. The equivalence ratio is $\phi = 1$ and the Reynolds number is $Re = 10500$.

The u_{RMS} value of the flame front at $y^+ = 16.4$ corresponds to the u_{RMS} value where the solid black line representing $y^+ = 16.4$ and the measured u_{RMS} intersect in Figure 4.7a. The radial velocity fluctuation, v_{RMS}, was obtained in a similar fashion. Table 4.1 lists u_{RMS} and v_{RMS} for different obstruction heights, h_{obstr}, and for the 60, 80 and 100% H_2 cases. Flame angles were calculated using the flame front modelled with method 3. The flame angle is given by:

$$\alpha_f = tan^{-1}\left(\frac{r_2 - r_1}{x_2 - x_1}\right), \tag{4.4}$$

where r and x are the radial and axial coordinate of the flame front, respectively. The value for radial coordinate r_1 was determined at the axial station $x_1 \sim 0.1d$. The value for radial coordinate r_2 was determined at the axial station $x_2 \sim 1.3d$. The results are listed in Table 4.1.

		60% H_2				80% H_2				100% H_2			
	h_{obstr} (mm)	0	0.5	1	1.5	0	0.5	1	1.5	0	0.5	1	1.5
Exp.	$U_{FB,exp}$ (m/s)	4.93	5.00	5.35	6.27	8.06	8.57	9.54	10.56	14.26	14.74	16.29	18.02
Model	u_τ (m/s)	0.764	0.772	0.821	0.942	1.183	1.250	1.372	1.499	1.983	2.042	2.228	2.434
Model	y_{FB} (mm)	0.361	0.357	0.336	0.292	0.249	0.236	0.215	0.197	0.170	0.165	0.152	0.139
Method 3	x_{FF}/d (-)	0.40	0.38	0.36	0.34	0.38	0.36	0.32	0.30	0.32	0.29	0.28	0.26
Exp.	u_{RMS} (m/s)	0.80	0.84	0.92	0.98	1.42	1.50	1.50	1.58	2.28	2.40	2.50	2.55
Exp.	v_{RMS} (m/s)	1.66	1.69	1.69	1.67	2.70	2.65	2.55	2.60	4.63	4.65	4.68	4.44
Method 3	α_f (°)	14.33	14.44	14.7	15.63	13.88	14.21	14.69	15.43	15.98	16.41	16.77	17.38
-	S_l (m/s)	0.70				1.00				2.10			
Cantera	ν_u (m^2/s)	1.67e-5				1.80e-5				2.06e-5			

Table 4.1: Flame angles and velocity fluctuations in the flame front at $y^+ = 16.4$. The burner inner diameter is $d = 25.20$ mm, the laminar flame speed for the case 100% H_2 was modelled with Cantera, using the Ó Conaire reaction mechanism used in [Hoferichter et al., 2017b]. The other laminar flame speeds were extracted from [Chen, 2012]. The equivalence ratio is $\phi = 1$. In the first column it is stated how the parameter value was obtained. 'Exp.' means the value was determined experimentally.

The root mean square of the axial velocity, u_{RMS}, increases slightly with increasing obstruction height for all gas compositions. The root mean square of the radial velocity, v_{RMS}, remains constant, except for the case 100% H_2 where v_{RMS} decreases with increasing obstruction height. The flame angle increases with obstruction height for all gas compositions. The parameter values in Table 4.1 were used as input for the flashback prediction models discussed in the next section, section 4.4.

4.4 Prediction models

In this section the experimental results are compared to the results modelled with flashback prediction models developed at the Technical University of Munich. From now on, the model that predicts flashback of unconfined flames is referred to as the 'TU Munich unconfined model' and the model that predicts flashback of confined flames is referred to as the 'TU Delft confined model'. The TU Munich unconfined model is discussed in Section 4.4.1. To account for the obstruction height the TU Munich unconfined model was modified by a correction factor based on the experimental values of the flame angle. The TU Delft confined model is discussed in Section 4.4.2. The full set of equations describing both models is included in Appendix A and the Python script used to implement the TU Munich unconfined model is included in Appendix B. .

4.4.1 TU Munich unconfined model

The model in this section is similar to the model in [Hoferichter et al., 2017b]. The model uses flame angle theory to relate global and local properties, and models the turbulent burning velocity with the Damköhler correlation. The global and local analysis are related by:

$$U_{FB} = \frac{\overline{S}_t u(y_{FB})}{S_t(y_{FB})}, \tag{4.5}$$

where U_{FB} is the bulk velocity at flashback, $\overline{S}_t$ is the turbulent burning velocity averaged over the burner area, $u(y_{FB})$ is the gas axial velocity at wall distance y_{FB} and $S_t(y_{FB})$ is the turbulent burning velocity at y_{FB}.
The TU Munich unconfined model was replicated and verified with results published in [Hoferichter et al., 2017b], see Figure 4.8. The replicated model was used in the present research.

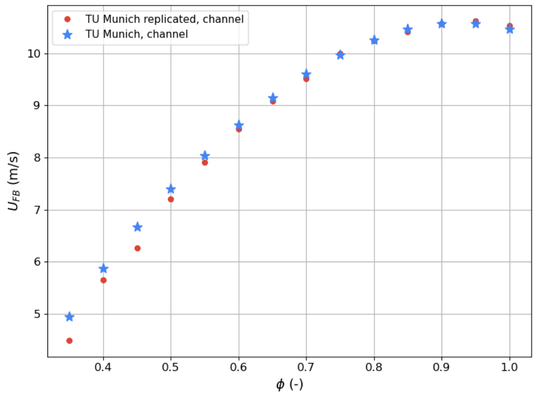

Figure 4.8: Comparison of the results modelled in the present research and the results in [Hoferichter et al., 2017b].

In the range $0.5 \leq \phi \leq 1.0$, the reproduced results are within 5% difference when compared to the results published by Hoferichter. Hoferichter did not publish modelled bulk velocities at flashback of flames produced by a tube burner, which is why in Figure 4.8 the 'channel' bulk velocities are shown. Next, the modelled results were compared to the experimental results of the present study, see Figure 4.9.

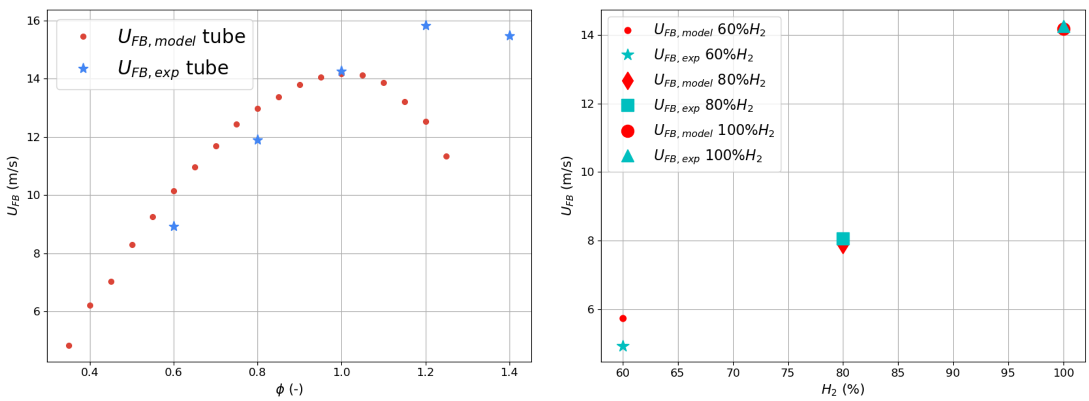

(a) Modelled and experimental U_{FB} for different ϕ for the case 100% H_2.

(b) Modelled and experimental U_{FB} for the cases 60, 80 and 100% H_2 for $\phi = 1$.

Figure 4.9: Modelled and experimental bulk velocities at flashback of a flame produced by a tube burner with $d = 25.20$ mm and $h_{obstr} = 0$ mm.

Figure 4.9a shows that the modelled results overpredict and underpredict the experimental results for $\phi < 1.0$ and $\phi > 1.0$, respectively. At stochiometric conditions the modelled and experimental bulk velocity at flashback have less than 1% difference. In this research the TU Munich unconfined model was used to model flames for $\phi = 1$. Figure 4.9b shows the modelled and experimental bulk velocities at flashback for the cases 60%, 80% and 100% H_2 and for $\phi = 1$. The difference between the experimental and modelled bulk velocity at flashback for the case 80% and 100% is 2.2% and less than 1%, respectively. For the case 60% H_2 the difference is 16.4%.
To account for the obstruction height in the TU Munich unconfined model it was attempted to use the experimental velocity fluctuations and flame angle. The experimental and modelled flame angle and velocity fluctuations for $h_{obstr} = 0$ mm are listed in Table 4.2.

	60% H_2	80% H_2	100% H_2
$\alpha_{FB,model}$ (°)	31.8	33.9	41.0
$\alpha_{f,exp}$ (°)	14.33	13.88	15.98
$u_{RMS,model}$ (m/s)	0.55	0.74	1.25
$u_{RMS,exp}$ (m/s)	0.80	1.42	2.28
$v_{RMS,exp}$ (m/s)	1.66	2.70	4.63

Table 4.2: The modelled and experimental flame angles and velocity fluctuations for the cases 60, 80 and 100% H_2 for $h_{obstr} = 0$ mm.

The modelled velocity fluctuations underpredict the experimental velocity fluctuations. Also, the experiment shows that the turbulence is anisotropic because $v_{RMS,exp}$ is about two times $u_{RMS,exp}$.
All modelled flame angles are two to three times the experimental flame angle. It was expected that the experimental flame angle would be smaller than the modelled flame angle because during the experiments U_{bulk} was set 0.5 to 1 m/s above U_{FB} to avoid flashback, and because the TU Munich unconfined model overpredicts flame angles to about 5°[Hoferichter et al., 2017b]. Faldella determined similar experimental flame angles as the experimental flame angles reported in the present research [Faldella, 2019].
To account for the obstruction height the TU Munich unconfined model was modified by substituting the modelled velocity fluctuations with the experimental values. However, it seems the TU Munich unconfined model does not allow for substituting experimental values into the model because when the experimental values of the velocity fluctuations were substituted for the modelled velocity fluctuations, the model would predict a non-physical relation between U_{FB} and u_{RMS}: the bulk velocity at flashback would decrease with increasing velocity fluctuations.
Because directly substituting the experimental values in the model did not result in an accurate prediction model, it was attempted to modify the model with a correction factor based on the experimental values. A modification with a correction factor based on the experimental flame angle, C_α, gave the best results. The TU Munich unconfined model was modified by changing:

$$U_{FB} = \overline{S}_{t,s}/\sin(\alpha_{FB,model}), \tag{4.6}$$

to:

$$U_{FB} = \overline{S}_{t,s}/\sin\left(\frac{\alpha_{FB,model}}{C_\alpha}\right), \tag{4.7}$$

where C_α is a correction factor for the flame angle and $\alpha_{FB,model}$ is the modelled flame angle at flashback. To account for the obstruction height in the model, C_α is given by:

$$C_\alpha = \frac{\alpha_{f,exp}}{\alpha_{f,exp}(h_{obstr} = 0\text{ mm})}, \tag{4.8}$$

where $\alpha_{f,exp}$ is the flame angle determined by experiments. The correction factor C_α is listed in Table 4.3 together with the experimental flame angle and the flame angle at flashback determined with the modified model.

	60% H_2				80% H_2				100% H_2			
h_{obstr} (mm)	0	0.5	1	1.5	0	0.5	1	1.5	0	0.5	1	1.5
C_α (−)	1.00	1.01	1.03	1.09	1.00	1.02	1.06	1.11	1.00	1.03	1.05	1.09
$\alpha_{FB,model}$ (°)	31.8	31.3	30.2	26.8	33.9	32.3	30.2	27.5	41.0	38.8	37.1	34.4
$\alpha_{f,exp}$ (°)	14.33	14.44	14.7	15.63	13.88	14.21	14.69	15.43	15.98	16.41	16.77	17.4

Table 4.3: Experimental and modelled flame angles and correction factor C_α for different gas compositions and obstruction heights. The modified TU Munich unconfined model was used to determine $\alpha_{FB,model}$ for $\phi = 1$ and $d = 25.20$ mm.

The increase in $\alpha_{f,exp}$ for increasing h_{obstr} might be explained as follows. During the experiments all parameters were kept constant except the obstruction height. Bulk velocity at flashback increases with increasing obstruction height. The closer the bulk velocity at flashback is to the bulk velocity, the closer the flame front is to the burner rim and the larger is the flame angle.
The decrease in $\alpha_{FB,model}$ with increasing h_{obstr} might be interpreted as follows. With increasing obstruction height the flashback propensity increases and the flame will already flashback for a smaller cone angle when compared to the case $h_{obstr} = 0$ mm.
The experimental and modelled results indicate that the experimental flame angle is not the flame angle at flashback. However, the experimental flame angles listed in Table 4.3 do show the effect of the obstruction height on the flame angle, so $\alpha_{f,exp}$ might be used to determine C_α and account for the obstruction height in the TU Munich unconfined model.

Table 4.4 lists the modelled bulk velocity at flashback determined with the modification as proposed in Eq. 4.6 - 4.8, the bulk velocity at flashback determined by the experiments and the difference between the experimental and modelled bulk velocity at flashback.

	60% H_2				80% H_2				100% H_2			
h_{obstr} (mm)	0	0.5	1	1.5	0	0.5	1	1.5	0	0.5	1	1.5
$U_{FB,exp}$ (m/s)	4.93	5.00	5.35	6.27	8.06	8.57	9.54	10.56	14.26	14.74	16.29	18.02
$U_{FB,model}$ (m/s)	5.74	5.87	6.18	7.43	7.88	8.45	9.33	10.82	14.17	15.29	16.31	18.22
ΔU_{FB} (%)	16.4	17.4	15.5	18.5	2.23	1.40	2.20	2.40	6.31e-3	3.73	1.23e-3	1.11

Table 4.4: Bulk velocities at flashback determined by the TU Munich unconfined model with the modification as proposed in Eq. 4.6 - 4.8 and the bulk velocities at flashback as determined by experiments.

The difference between modelled and experimental velocity, ΔU_{FB}, is given by:

$$\Delta U_{FB} = 100\frac{|U_{FB,model} - U_{FB,exp}|}{U_{FB,exp}}. \tag{4.9}$$

For the case 60% H_2, the largest difference between the experimental and modelled bulk velocity at flashback is 18.5% for $h_{obstr} = 1.5$ mm. For the case 80% H_2, the largest difference between $U_{FB,exp}$ and $U_{FB,model}$ is 2.40% for $h_{obstr} = 1.5$ mm and for the case 100% H_2, the largest difference between $U_{FB,exp}$ and $U_{FB,model}$ is 3.73% for $h_{obstr} = 0.5$ mm. Hence, the largest difference between $U_{FB,exp}$ and $U_{FB,model}$ for all cases in Table 4.4 is 18.5%. The largest difference between $U_{FB,exp}$ and $U_{FB,model}$ for the cases 60%, 80% and 100% H_2 and zero obstruction height is 16.4%. Thus, the modification predicts the effect of obstruction height on bulk velocity at flashback while increasing the maximum difference between modelled and experimental bulk velocity with 2.1% for the cases 60%, 80% and 100% H_2 for $\phi = 1$. Figure 4.10 shows the experimental and modelled bulk velocity at flashback for the cases 60%, 80% and 100% H_2 for different values of the dimensionless obstruction height, h_{obstr}/D.

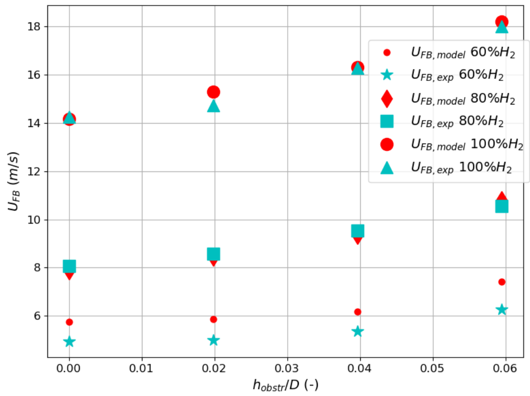

Figure 4.10: Experimental bulk velocities at flashback and bulk velocities at flashback modelled with the modification given in Eq. 4.7 for the cases 60%, 80% and 100% H_2 as a function of the dimensionless obstruction height, h_{obstr}/D for $\phi = 1$.

The modelled and experimental results show the same dependence on obstruction height h_{obstr}. The similarity in modelled and experimental results indicates that flashback might be described by average flame properties and flow characteristics and indicates that turbulent burning velocity is a critical parameter in the flashback process of premixed unconfined flames. Furthermore, Figure 4.10 indicates that flame angle plays a critical role in the TU Munich unconfined model, e.g. for the case 100% H_2 and $h_{obstr} = 1.5$ mm the flame angle correction is 9% and the corrected bulk velocity at flashback is 28% larger than the uncorrected bulk velocity at flashback.

4.4.2 TU Delft confined model

In the TU Delft confined model it is assumed that flashback occurs at the onset of boundary layer separation. The Stratford criterion is used to asses if the boundary layer separates. The turbulent burning velocity, S_t, is modelled with the Damköhler correlation. Table 4.5 lists the experimental and modelled bulk velocities at flashback for the cases 60%, 80% and 100% H_2 for $h_{obstr} = 0$ mm.

	60% H_2	80% H_2	100% H_2
$U_{FB,exp}$ (m/s)	4.93	8.06	14.26
$U_{FB,model}$ (m/s)	21.22	31.10	41.95

Table 4.5: Experimental and modelled bulk velocities at flashback for the cases 60%, 80% and 100% H_2 for $h_{obstr} = 0$ mm. The flames analyzed have an equivalence ratio of $\phi = 1$ and the burner inner diameter is $d = 25.20$ mm.

The bulk velocity at flashback determined with the TU Delft confined model, $U_{FB,model}$, is more than 2.9 times the experimental bulk velocity at flashback, $U_{FB,exp}$, for all gas compositions. The results show that flame confinement is vital to the flashback process and indicate that as soon as a flame produced by a tube burner travels upstream past the burner rim, locally changing flame confinement to a confined set-up, flashback will occur. Other than the velocity fluctuations in the flame front, coldflow velocity fluctuations were also used as input in the TU Delft confined model. The bulk velocities at flashback determined with the coldflow fluctuations were similar to $U_{FB,model}$ in Table 4.5, with a maximum difference of 10%.
The results discussed in Section 4.4.1 and 4.4.2 indicate that the turbulent burning velocity plays a critical role in the flashback process of premixed unconfined flames. As soon as the turbulent burning velocity is larger than the local gas velocity component normal to the flame front, the flame travels upstream. When the flame travels past the burner

rim, the flame confinement locally changes to a confined set-up, the flashback propensity increases and flashback occurs.

4.5 Low velocity streaks

Eichler states that the combined effect of low velocity streaks and an adverse pressure gradient caused by the flame front is dominant in the flashback process [Eichler et al., 2012]. The effect of an adverse pressure gradient is shown in Figure 4.11.

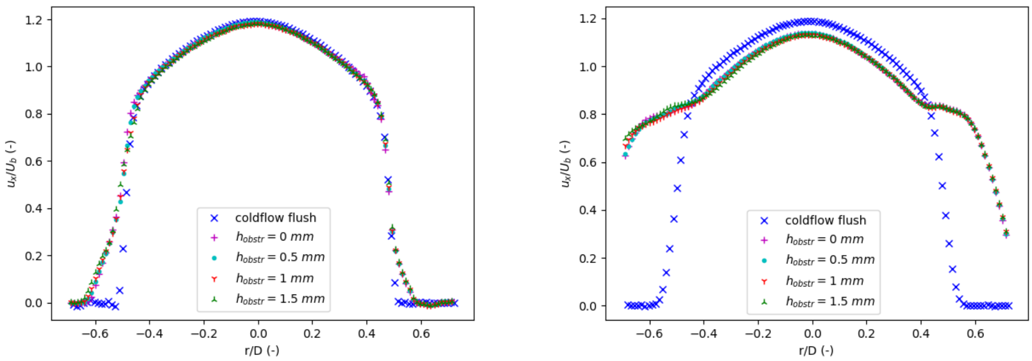

(a) Mean velocity profile of the axial component, 1 mm downstream the burner exit. *(b) Mean velocity profile of the axial component, 8 mm downstream the burner exit.*

Figure 4.11: Mean velocity profile of the axial component for the case 60% H_2 for different obstruction heights, h_{obstr}, and for $\phi = 1$ produced by a tube burner with $d = 25.20$ mm.

For $|r/D| \leq 0.5$ the mean velocity profile decreases with increasing downstream distance due to the adverse pressure gradient.
Histograms of the instantaneous velocity were made to gain insight in the occurrence of low velocity streaks. For each gas composition and for $r/D < 0$ histograms were made at 3, 6, 9 and 12 mm downstream the burner exit and just upstream of the contour for $U_{RMS} = 1.1$ m/s in Figure 4.12.

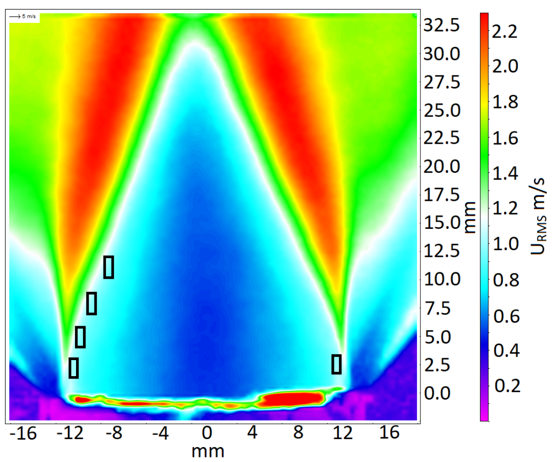

Figure 4.12: Root Mean Square of the velocity field for the case 60% H_2, $\phi = 1$ and h_{obstr} = 0 mm produced by a Bunsen burner with 25.20 mm inner diameter.

The black rectangles in Figure 4.12 show the areas where histograms were made. The downstream distances were chosen because the flashback experiments indicate that flashback initiates at a distance 8-12 mm downstream the burner exit and because the distances closer to the burner rim include or are in the vicinity of $y^+ = 16.4$. For 60%

H_2 the procedure was repeated, only now for $r > 0$ to compare the instantaneous velocity downstream of an obstructed boundary layer and a normal boundary layer.
Low velocity streaks upstream a flame front, that is relatively far upstream are of particular interest because it is likely that flashback initiates at a time instant when the instantaneous axial velocity is low. The upstream flame front shape was approached by assuming that the flame front is located where, at a fixed axial station, U_{RMS} is 1.9 times the minimum RMS of the velocity at that axial station.
None of the histograms showed any relation between boundary layer obstruction and low velocity streaks. That is, the shape of the histogram is independent of obstruction height. In fact nine histograms showed, by approximation, that obstruction height has no effect on the velocity distribution at all. Four histograms, all of which were constructed for $r/D < 0$, showed a difference in mean velocity. The details of the histograms that showed a difference: 3 mm downstream the burner exit for all gas compositions and 6 mm downstream the burner exit for the case 60% H_2. The histograms constructed 3 mm downstream the burner exit for the case 60% H_2 are shown in Figure 4.13.

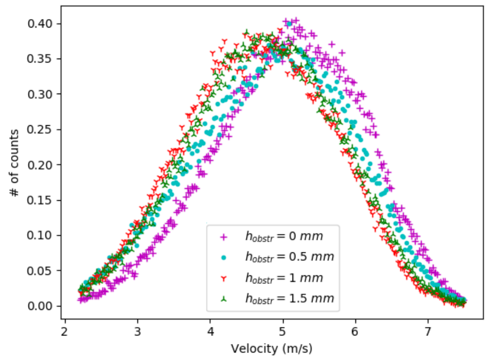

(a) Velocity histogram taken at 3 mm downstream of the burner exit and 13 mm downstream the BL obstruction for different values of h_{obstr}.

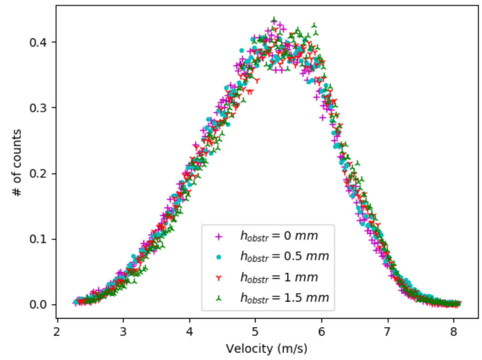

(b) Velocity histogram taken at 3 mm downstream of the burner exit on the side of the burner without BL obstruction for different values of h_{obstr}.

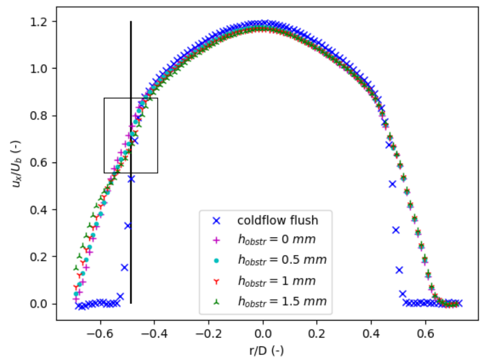

(c) mean velocity profile 3 mm downstream the burner exit.

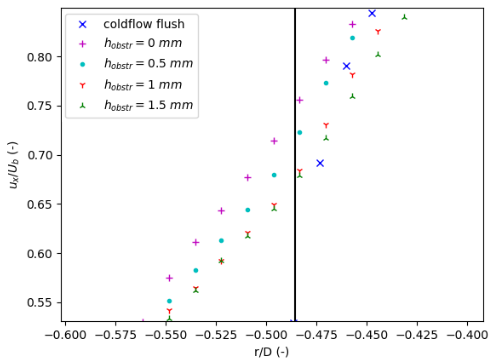

(d) Zoom of Figure 4.13c.

Figure 4.13: Histograms and mean velocity profiles for different obstruction heights, h_{obstr}, for the case 60% H2, d = 25.20 mm, Re = 10500, U_{bulk} = 7.1 m/s and $\phi = 1$. The black rectangle in 4.13c marks the boundaries of 4.13d.

The histogram shifts to lower velocities with increasing obstruction height, h_{obstr}, see Figure 4.13a. However, the histogram shape remains the same. Thus, the results show that obstruction height has no effect on low velocity streaks.
If the mean velocity decreases with increasing obstruction height this should be captured by

the mean velocity profile too. Figures 4.13c and 4.13d show the mean velocity profile and a zoom of the velocity profile, respectively, at the same axial station were the histograms were taken. Figure 4.13d shows that mean velocity locally decreases with increasing obstruction height, consistent with the results shown in Figure 4.13a.
A histogram was also made in the unobstructed boundary layer, see Figure 4.13b. In the unobstructed boundary layer the obstruction height has no effect on the histogram shape and histogram peak location. The other histograms that showed any effect of obstruction height were included in Appendix F.
The results in this section indicate that the flashback process of unconfined flames is different than the flashback process of confined flames.

4.6 Flashback process

The flashback process was investigated by experiments described in Section 3.5.3. The flashback process of a flame produced by a Bunsen burner without boundary layer obstruction is characterized by five steps that are listed below.

1. initiation around 8-12 mm downstream the burner exit.
2. radial inward flame front propagation, resulting in a sphere-like structure in the flame front.
3. upstream flame front propagation, with a clear flame front leading tip.
4. upstream flame front propagation past the burner rim.
5. Full flashback.

The five steps are visualized in Figure 4.14.

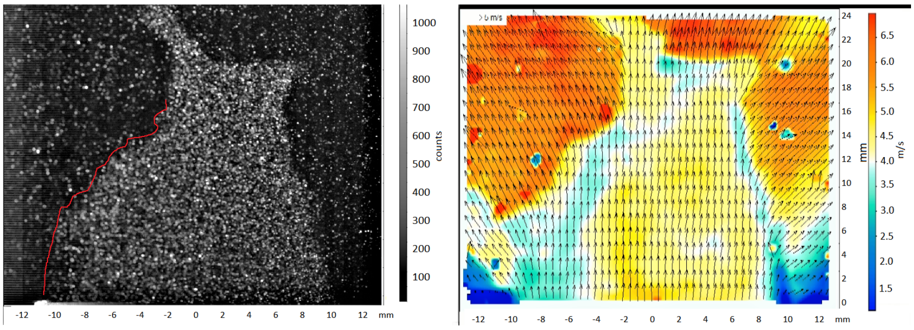

(a) Flashback process step 1, $t = 0$ ms.

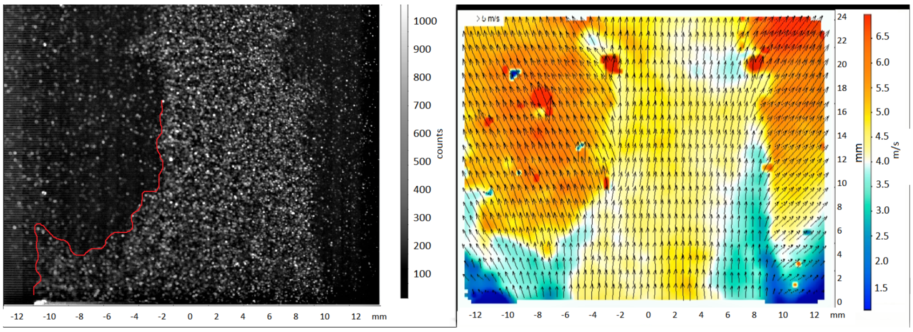

(b) Flashback process step 2, $t = 3$ ms.

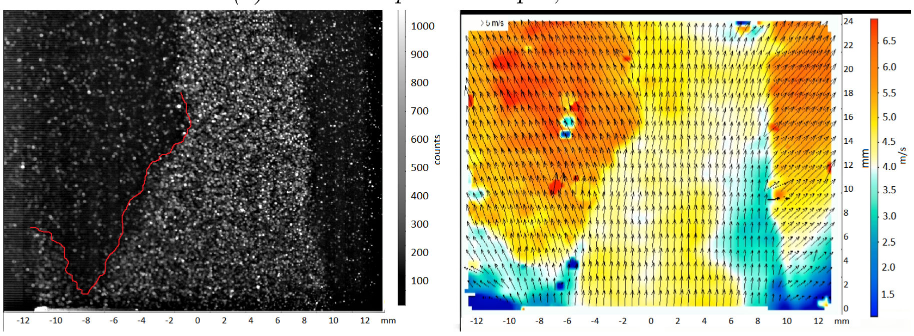

(c) Flashback process step 3, $t = 3.9$ ms.

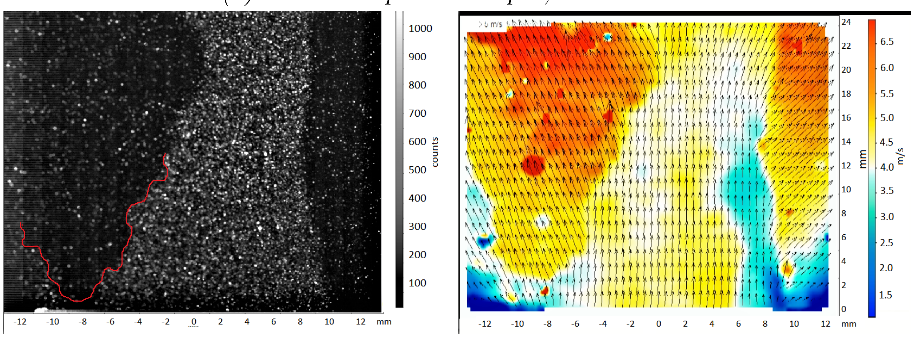

(d) Flashback process step 4, $t = 4.2$ ms.

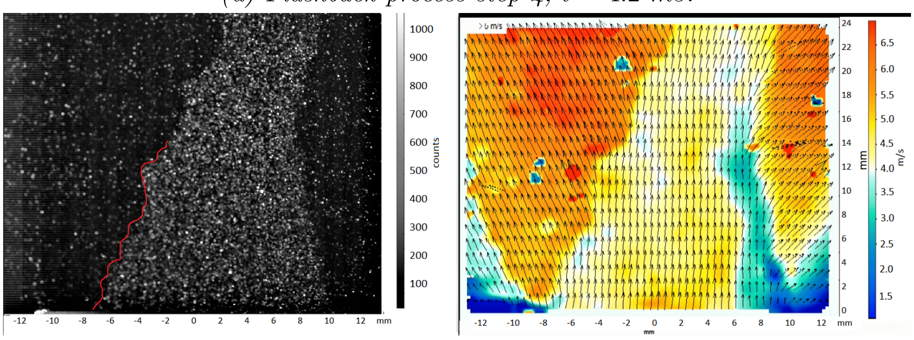

(e) Flashback process step 5, $t = 4.8$ ms.

Figure 4.14: Visualization of the flashback process for the case 40% H_2, $h_{obstr} = 1$ mm and $\phi = 1$. The laser frequency is 10 kHz. All figures show the raw PIV images on the left hand side and the processed velocity field on the right hand side.

The 0%, 40%, 50% and 100% H_2 cases were studied for different obstruction heights and in all cases the location of propagation was clear. If the flow was subject to an obstruction, the flame leading tip propagated in the domain $r/D < -0.35$, except in one experiment where flashback seemed to happen in the core. If the flow was not subject to an obstruction, flame leading tip propagation occurred at a random location along the circumference of the burner rim.
Figure 4.15 shows that the flashback process (the five steps described before) depends on the boundary layer obstruction.

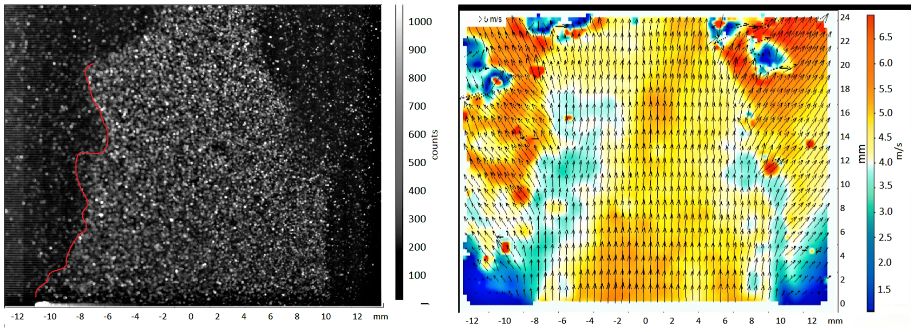

(a) *Stable flame close to flashback,* $U_{bulk} = 3.80\ m/s$.

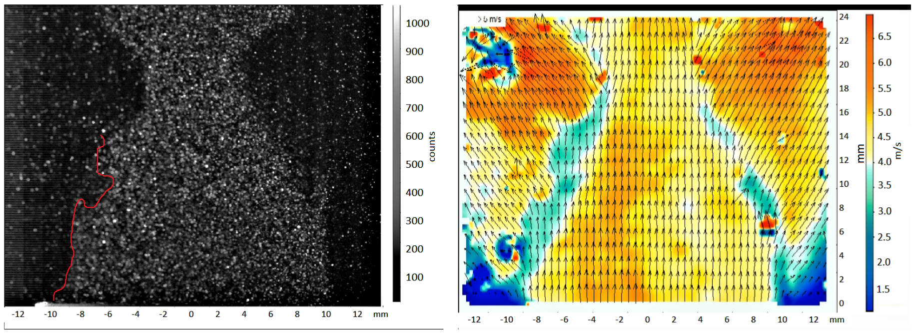

(b) *Stable flame close to flashback,* $U_{bulk} = 3.72\ m/s$.

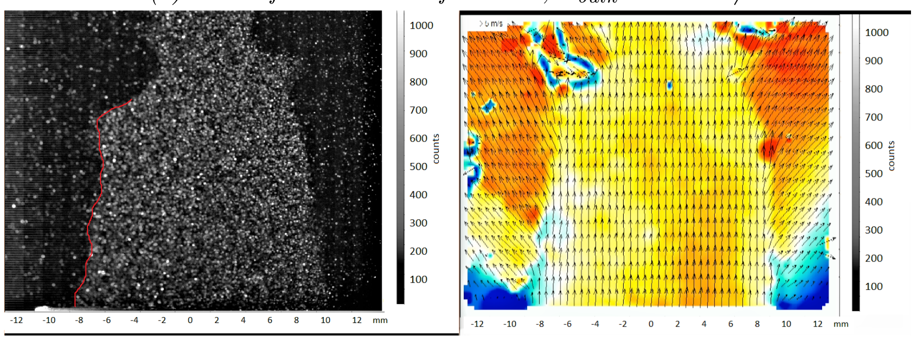

(c) *Flame at the onset of flashback with part of the flame inside the burner,* $U_{bulk} = 3.66\ m/s$.

Figure 4.15: The effect of the boundary layer obstruction on the flashback process for the case 40% H_2, $\phi = 1$, $h_{obstr} = 1$ *mm. The burner inner diameter is d = 19.76 mm.*

Figure 4.15 shows the flashback process of a flame produced by a Bunsen burner with obstruction height $h_{obstr} = 1$ mm. Instead of the five steps described before, now three clear steps can be distinguished in the flashback process:

1. While the flame is still stable, the flame downstream the boundary layer obstruction is very close to the the burner rim.

2. While the flame is still stable, the flame downstream the boundary layer obstruction is upstream the burner rim and seems to anchor on the obstruction.

3. Flashback initiates at the obstruction.

The flame shown in Figures 4.15a and 4.15b will not flashback further even though part of the flame front is very close to, or already inside, the burner. The flame in Figure 4.15c is at the onset of flashback. Flame shapes as shown in Figure 4.15c were not observed if smooth burner walls were used, indicating that the obstruction functions as flame anchor point. Thus, the flashback process of a flame produced by a Bunsen burner with boundary layer obstruction is different to the flashback process of a flame produced by a tube burner with smooth walls.

5 Conclusion

In this study the flashback mechanism of premixed turbulent unconfined hydrogen and hydrocarbon flames was investigated by varying velocity fluctuations while keeping bulk velocity constant. A mechanical obstruction was placed in the boundary layer to locally disturb the flow and alter velocity fluctuations. Hydrogen/DNG/air mixtures with a fuel composition of 0%, 20%, 40%, 60%, 80% and 100% H_2 were studied for equivalence ratios in the range 0.6 - 1.4. Particle Image Velocimetry was used to obtain velocity data of the non-reacting and reacting flow. Three research objectives were formed:

- Gain insight in the relation between turbulent velocity fluctuations and bulk velocity at flashback.
- Gain insight in the relation between low velocity streaks upstream the flame front and bulk velocity at flashback.
- Gain insight in the relation between flame front location, boundary layer obstruction and bulk velocity at flashback.

The bulk velocity at flashback, U_{FB}, the turbulent velocity fluctuations, u', and the flame angle, α_f, increased with increasing boundary layer obstruction height for all gas mixtures studied in the present research. The flame front axial distance from the burner rim decreased with increasing obstruction height, indicating that a flame produced by a burner with obstruction is more prone to flashback and confirming the observed relation between obstruction height and bulk velocity at flashback.
If the boundary layer was obstructed, flashback would always initiate downstream the obstruction. During some experiments the flame seemed to anchor on the obstruction, locally changing flame confinement to a confined set-up.

For the cases 60%, 80% and 100% H_2, the experimentally determined U_{FB}, u' and α_f were compared to U_{FB}, u' and α_f determined by flashback prediction models of premixed confined and premixed unconfined flames developed at the Technical University of Munich. The confined model overestimates the experimentally determined bulk velocities at flashback for all gas mixtures, indicating that when the flame leading tip is located upstream the burner exit, which is the case when the flame anchors on the obstruction, flashback propensity increases. The difference between the bulk velocities at flashback determined by the unconfined model and by the experiments is 16.4%, 2.20% and 6.31e-3% for the case 60%, 80% and 100% H_2, respectively.
To account for the obstruction two modifications were introduced to the unconfined model:

- The experimental velocity fluctuations were substituted with the modelled velocity fluctuations. With this modification the unconfined model predicted a decreasing bulk velocity at flashback for increasing velocity fluctuations. Hence, this modification did not improve the model.
- The modelled flame angle was corrected with a correction factor based on the experimentally determined flame angle. The modified model and the experiments show

similar bulk velocities at flashback for all gas mixtures and obstruction heights, with a maximum difference of 18.5%. The maximum difference for the case with smooth burner walls is 16.4% so the implemented modification adds 2.1% to the maximum difference while predicting the effect of obstruction height on the bulk velocity at flashback.

The similarity between the modelled and the experimental bulk velocity at flashback indicates that flashback of premixed turbulent unconfined flames is caused by an imbalance between the local turbulent burning velocity and the local gas velocity. Furthermore, the similarity indicates that flashback, despite it's transient nature, might be modelled with time-averaged flow characteristics.
While causing the bulk velocity at flashback to increase, the boundary layer obstruction had no effect on the occurrence of low velocity streaks just upstream the flame front, indicating that, for premixed turbulent unconfined flames, the combined effect of an adverse pressure gradient and low velocity streaks on the bulk velocity at flashback is not as large as the combined effect of an adverse pressure gradient and low velocity streaks on U_{FB} of premixed turbulent confined flames.

The absence of low velocity streaks and the similarity between the modelled and the experimental bulk velocity at flashback, when the model is adjusted with the second modification, indicate that the flashback process of premixed turbulent unconfined flames is different to the flashback process of premixed turbulent confined flames and indicate that turbulent burning velocity is a critical parameter in the flashback process of premixed turbulent unconfined flames.

Recommendations

- The modification implemented in the unconfined model is yet based on the experiments and to gain more insight in the effect of a boundary layer obstruction on the flashback propensity it is recommended to model the correction factor.
- To control the flashback location of a flame produced by a tube burner it is recommended to locally change burner wall temperature.
- Flame angle seems to be an important parameter in the flashback process of unconfined flames and might be used as indicator for flashback prevention systems. It is therefore recommended to investigate the possibilities of continuously measuring the flame angle.
- Closely related to the previous item: the flame front location is also a parameter critical in the flashback process and, in order to develop a flashback prevention system, it is recommended to investigate the possibilities of continuously measuring the flame front location.
- The results in the present research indicate that the flashback process of premixed turbulent unconfined flames is different to the flashback process of premixed turbulent confined flames. The results raise the question: Is the flashback process of premixed turbulent enclosed flames a combination of the unconfined and confined flashback processes, or is it a completely different process? To gain more insight on flashback it is recommended to investigate premixed turbulent flames in an enclosed set-up.

Bibliography

[Baumgartner, 2014] Baumgartner, G. (2014). *Flame Flashback in Premixed Hydrogen-Air Combustion Systems*. PhD thesis, Technische Universität Munchen.

[Baumgartner et al., 2016] Baumgartner, G., Boeck, L. R., and Sattelmayer, T. (2016). Experimental Investigation of the Transition Mechanism from Stable Flame to Flashback in a Generic Premixed Combustion System with High-Speed Micro-Particle Image Velocimetry and Micro-PLIF Combined with Chemiluminescence Imaging. *Journal of Engineering for Gas Turbines and Power*, 138(2):1–10.

[Bechtold and Matalon, 2001] Bechtold, J. K. and Matalon, M. (2001). The dependence of the Markstein length on stoichiometry. *Combust. Flame*, 127:1906–1913.

[Björnsson, 2019] Björnsson, O. H. (2019). Boundary layer flashback prediction for low emissions full hydrogen gas turbine burners using flow simulation.

[Chen, 2012] Chen, Z. (2012). A model for the laminar flame speed of binary fuel blends and its application to methane/hydrogen mixtures. *International Journal of Hydrogen Energy*, 37(13):10380–10389.

[Eichler et al., 2012] Eichler, C., Baumgartner, G., and Sattelmayer, T. (2012). Experimental investigation of turbulent boundary layer flashback limits for premixed hydrogen-air flames confined in ducts. *Journal of Engineering for Gas Turbines and Power*, 134(1):1–8.

[Eichler and Sattelmayer, 2011] Eichler, C. and Sattelmayer, T. (2011). Experiments on flame flashback in a quasi-2D turbulent wall boundary layer for premixed methane-hydrogen-air mixtures. *Journal of Engineering for Gas Turbines and Power*, 133(1):1–7.

[Eichler and Sattelmayer, 2012] Eichler, C. and Sattelmayer, T. (2012). Premixed flame flashback in wall boundary layers studied by long-distance micro-PIV. *Experiments in Fluids*, 52(2):347–360.

[Faldella, 2019] Faldella, F. (2019). Experimental investigation of Boundary Layer Flashback in high H2 concentration turbulent premixed jet flames.

[Gruber et al., 2012] Gruber, A., Chen, J., Valiev, D., and Law, C. (2012). Direct Numerical Simulation of Premixed Flame Boundary Layer Flashback in Turbulent Channel Flow. *Journal of Fluid Mechanics*, (709):516–542.

[Hanania and Donev, 2020] Hanania, J. and Donev, J. (2020). Primary Energy.

[Hoferichter et al., 2017a] Hoferichter, V., Hirsch, C., and Sattelmayer, T. (2017a). Analytic prediction of unconfined boundary layer flashback limits in premixed hydrogen–air flames. *Combustion Theory and Modelling*, 21(3):382–418.

[Hoferichter et al., 2017b] Hoferichter, V., Hirsch, C., and Sattelmayer, T. (2017b). Prediction of Confined Flame Flashback Limits Using Boundary Layer Separation Theory. *Journal of Engineering for Gas Turbines and Power*, 139(2):1–10.

[IEA, 2019] IEA (2019). Renewables Information 2019.

[Kahan, 2019] Kahan, A. (2019). Energy Information Administration.

[Kalantari and McDonell, 2017] Kalantari, A. and McDonell, V. (2017). Boundary layer flashback of non-swirling premixed flames: Mechanisms, fundamental research, and recent advances. *Progress in Energy and Combustion Science*, 61:249–292.

[Kirubakaran et al., 2009] Kirubakaran, A., Jain, S., and Nema, R. (2009). Renewable and Sustainable Energy Reviews. *Elsevier*, 13(9):2430–2440.

[Law, 2006] Law, C. K. (2006). *Combustion Physics.* Campridge University Press, New York.

[Lewis and von Elbe, 1943] Lewis, B. and von Elbe, G. (1943). Stability and Structure of Burner Flames. *The Journal of Chemical Physics*, 11(2):75–97.

[Lindsey and Dahlman, 2020] Lindsey, R. and Dahlman, L. (2020). Climate Change: Global Temperature.

[Meneveau and Poinsot, 1991] Meneveau, C. and Poinsot, T. (1991). Stretching and quenching of flamelets in premixed turbulent combustion. pages 311–332.

[Nieuwstadt et al., 2015] Nieuwstadt, F. T. M., Boersma, B. J., and Westerweel, J. (2015). *Turbulence.* Springer.

[ÓConaire et al., 2004] ÓConaire, M., Curran, H., Simmie, J., Pitz, W., and Westbrook, C. (2004). A Comprehensive modeling study of hydrogen oxidation. *International Journal of Chemical Kinetics*, 36:603–622.

[Peters, 2000] Peters, N. (2000). Turbulent Combustion.

[Pope, 2000] Pope, S. (2000). Turbulent Flows. *Cambridge University Press.*

[Putnam and Jensen, 1949] Putnam, B. A. A. and Jensen, R. A. (1949). Application of dimensionless numbers to flashback and other combustion phenomena. pages 89–98.

[Ramanathan and Feng, 2009] Ramanathan, V. and Feng, Y. (2009). Air pollution, greenhouse gases and climate change: Global and regial perspectives. *Elsevier*, 43(Atmospheric Environment):37–50.

[Richards, 2001] Richards, G. A. (2001). Issues for low-emission, fuel-flexible power systems. *Progress in Energy and Combustion Science*, 27:141–169.

[Richie, 2019] Richie, H. (2019). Renewable energy.

[Sánchez and Williams, 2014] Sánchez, A. L. and Williams, F. A. (2014). Recent advances in understanding of flammability characteristics of hydrogen. *Progress in Energy and Combustion Science*, 41(1):1–55.

[Somerscales, 1981] Somerscales, E. (1981). Fluid Dynamics. In *volume 18.*

[Tay-Wo-Chong et al., 2009] Tay-Wo-Chong, L., Komarek, T., Zellhuber, M., Lenz, J., Hirsch, C., and Polifke, W. (2009). Influence of Strain and Heat loss of Flame stabilization in a non-Adiabatic Combustor. In *European Combustion Meeting*, pages 1–6.

[Tober, 2019] Tober, J. (2019). Boundary layer flashback prediction of a low emission full hydrogen burner for gas turbine applications. *Master Thesis.*

[Tropea, 2007] Tropea, C. (2007). *Springer Handbook of Experimental Fluid Mechanics.*

[Tummers et al., 2011] Tummers, M. J., Jacobse, J., and Voorbrood, S. G. (2011). Turbulent flow in the near field of a round impinging jet. *International Journal of Heat and Mass Transfer*, 54(23-24):4939–4948.

[Warnatz et al., 1999] Warnatz, J., Maas, U., and Dibble, R. (1999). Combustion: Physical and Chemical Fundamentals, Modeling and Simulation, Experiments, Pollutant Formation. *Springer*, 2nd editio.

Appendices

A Prediction models

1 TU Munich unconfined model

The flashback prediction model described in this Appendix is developed at the Technical University of Munich and from now on, the model will be referred to as the TU Munich unconfined model. The model uses flame angle theory to relate global and local properties. The Damköhler correlation for small scale turbulence is used to model turbulent burning velocity, S_t.

Local analysis

Flame angle theory is used to relate turbulent burning velocity and gas velocity according to:

$$S_{t,s}(y_{FB}) = u(y_{FB})\sin(\alpha_{FB}), \tag{5.1}$$

where $S_{t,s}$ is the stretched turbulent burning velocity, u is the gas axial velocity and α_f is the flame angle. The wall normal distance of flashback initiation is y_{FB}. The wall normal distance is given by:

$$y = \frac{y^+\nu_u}{u_\tau}, \tag{5.2}$$

where ν_u is the kinematic viscosity of the unburned gas, u_τ is the shear velocity and y^+ is the normalized wall distance. It is assumed that flashback is initiated along the streamline of maximum turbulent burning velocity which is $y^+ = 16.4$ for premixed confined flames [Hoferichter et al., 2017b]. This finding is supported by Gruber [Gruber et al., 2012]. Baumgartner found for unconfined flame flashback that wall distances of flashback initiation are in the same range as $y^+ = 16.4$ [Baumgartner et al., 2016]. The shear velocity is given by:

$$u_\tau^2 = 0.03955\overline{U}_{FB}^{\frac{7}{4}}\nu_u^{\frac{1}{4}}d^{-\frac{1}{4}}. \tag{5.3}$$

Equation 5.3 is a model for fully developed non-reacting pipe flow.
In equation 5.1 the stretched turbulent burning velocity is modelled with the Damköhler correlation for small scale turbulence. The Damköhler correlation is given by:

$$S_{t,s} = S_{l,s}[1 + 2.3\left(\frac{u'}{S_{l,s}}\right)^{0.5}], \tag{5.4}$$

where $S_{l,s}$ is the stretched laminar burning velocity and u' is the velocity fluctuation. Hoferichter assumes that turbulence is isotropic. The stretched laminar burning velocity is given by:

$$S_{l,s} = S_l - l_m\kappa, \tag{5.5}$$

Where S_l is the laminar burning velocity. The laminar burning velocity is determined with the reaction mechanism of Ó Conaire [ÓConaire et al., 2004]. In Eq. 5.5 l_m is the

Markstein length and κ is flame stretch rate. Hoferichter models Markstein according to:

$$
\begin{aligned}
l_m &= \delta_l(\beta - (\sigma - 1)\frac{\gamma_1}{\sigma}, \\
\beta &= \gamma_1 + 0.5Ze(Le - 1)\gamma_2, \\
\gamma_1 &= \sigma, \qquad \gamma_2 = 1,
\end{aligned} \tag{5.6}
$$

where Le is the Lewis number. The Lewis number is the ratio of thermal and species diffusion. If the Lewis number is less than unity it might lead to thermal-diffusive instabilities. Hoferichter models Le according to:

$$Le = 1 + \frac{Le_{O2} - 1 + B(Le_{H2} - 1)}{1 + B}, \tag{5.7}$$

where B is given by:

$$B = 1 + Ze(\frac{1}{\phi} - 1). \tag{5.8}$$

The Zel'dovich number, Ze, is the ratio of the activation energy over the burned gas temperature times the universal gas constant. Typical values used for E_a are in the range 20 - 40 kcal/mol. The Zel'dovich number is given by:

$$Ze = \frac{E_a}{RT_b}, \tag{5.9}$$

where E_a is the activation energy, R is the gas constant and T_b is the temperature of the burned gas. In equation 5.5 flame stretch rate κ is modelled according to:

$$\kappa(y_{FB}) = \frac{2}{3}\Gamma_k \frac{u'(y_{FB})}{l_0} + \frac{1}{2}\frac{u'(y_{FB})}{l_0}, \tag{5.10}$$

where l_0 is the turbulent integral length scale and u' the turbulent velocity fluctuations. The efficiency function, Γ_k, is used in the intermittent turbulent net flame stretch model described by Meneveau and Poinsot [Meneveau and Poinsot, 1991]. The efficiency function depends on velocity fluctuation and equivalence ratio. Hoferichter used $10 \leq \Gamma_k \leq 30$. The efficiency function is given by:

$$log_{10}(\Gamma_k) = -\frac{1}{s + 0.4}e^{-(s+0.4)} + [1 - e^{-(s+0.4)}]\left(\frac{2}{3}\left[1 - \frac{1}{2}e^{-(u'/S_l)^{1/3}}\right]s - 0.11\right), \tag{5.11}$$

with:

$$s = log_{10}\left(\frac{l_0}{\delta_f}\right), \tag{5.12}$$

where δ_f is the flame front thickness. The turbulent velocity fluctuations u' are given by:

$$u'(y_{FB}) = 1.5u_\tau. \tag{5.13}$$

Properties needed in this model are mixture density, dynamic viscosity, heat conductivity, specific heat and adiabatic flame temperature. For the case 60 and 80 % H_2 all properties were extracted from Cantera using a GRI3.0 model and for the case 100% H_2 the Ó Conaire reaction mechanism was used.

Global analysis

Bulk velocity at flashback is determined by:

$$U_{FB} = \frac{\overline{S}_t}{\sin(\alpha_f)}, \tag{5.14}$$

where U_{FB} is the bulk velocity at flashback, α_f is the flame angle and $\overline{S}_t$ is the turbulent burning velocity averaged over the burner area. The averaged turbulent burning velocity is given by:

$$\overline{S}_{t,s} = \overline{S}_{l,s}[1 + 2.3\left(\frac{u'_{avg}}{\overline{S}_{l,s}}\right)^{0.5}], \tag{5.15}$$

where u'_{avg} is the turbulent velocity fluctuation averaged over the burner area. The averaged turbulent burning velocity is modeled in a similar fashion as the turbulent burning velocity, $S_{t,s}$, the difference being that u'_{avg} instead of $u'(y_{FB})$ is used.
The model was modified with the experimental data by correcting the flame angle α_f with a correction factor α_{corr}. The correction factor is given by:

$$\alpha_{corr} = \frac{\alpha_{f,exp}}{\alpha_{f,exp}(h_{obstr} = 0 \text{ mm})}, \tag{5.16}$$

where $\alpha_{f,exp}$ is the global flame angle determined by experiments. The values for α_f are listed in Table 4.1.

2 TU Delft confined model

The Stratford criterion is obtained semi-empirically [Hoferichter et al., 2017a] and under the condition of fully developed incompressible flow the Stratford criterion is given by:

$$\sqrt{2}\left(\frac{2\Delta p}{\rho_u(U_{FB,center})^2}\right)^{\frac{3}{2}} = 0.39, \tag{5.17}$$

where ρ_u is the unburned gas density, Δp is the pressure gradient and $U_{FB,center}$ is the centerline velocity at flashback. The pressure gradient is given by:

$$\Delta p = \rho_u S_{t,s}^2(\sigma - 1), \tag{5.18}$$

where σ is the ratio of unburned ans burned gas density and $S_{t,s}$ is the stretched turbulent burning velocity. The burning velocity is modelled with the Damköhler correlation for small scale turbulence, see the TU Munich unconfined model for the Damköhler correlation. Only the expression for the velocity fluctuations changes to:

$$u' = 2.6u_\tau, \tag{5.19}$$

where u_τ is the shear velocity and is given by:

$$u_\tau^2 = 0.03955\overline{U}_{FB}^{\frac{7}{4}}\nu_u^{\frac{1}{4}}d^{-\frac{1}{4}}. \tag{5.20}$$

Eq. 5.20 is a model for fully developed turbulent pipe flow and does not include combustion effects. In contrast to the TU Munich unconfined model, anisotropic turbulence effects are taken into account in the TU Delft confined model by modelling flame stretch rate κ according to:

$$\kappa = -\frac{\overline{u'v'}}{2k}\frac{\partial \overline{u}}{\partial y} + \Gamma_K\frac{\epsilon}{k}, \tag{5.21}$$

where ϵ is the turbulent dissipation rate and is $\epsilon = \frac{u'v'w'}{l_0}$, k is the turbulent kinetic energy and is $k = \frac{1}{2}\left(\overline{u'u'} + \overline{v'v'} + \overline{w'w'}\right)$ and $\overline{u'v'}$ is the Reynolds shear stress [Björnsson, 2019]. The efficiency function, Γ_k, was modelled with Eq. 5.11. In Eq. 5.17 the centerline velocity at flashback is given by::

$$U_{FB,center} \approx U_{FB} + 2.4u_\tau, \tag{5.22}$$

where U_{FB} is the bulk velocity at flashback. Eq. 5.22 was introduced by Pope for channel flow [Pope, 2000]. In the models it is assumed that Eq. 5.22 holds for pipe flow. Rewriting Eq. 5.17 gives:

$$U_{FB} = \left(2\left(\frac{0.39}{\sqrt{2}}\right)^{-\frac{2}{3}}\frac{\Delta p}{\rho_u}\right)^{\frac{1}{2}} - 2.4u_\tau. \tag{5.23}$$

B TU Munich unconfined model Python script

The first section shows the Python script of the replicated, unmodified TU Munich unconfined model for different equivalence ratios for the case 100% H_2. The second section shows the Python script of the modified TU Munich unconfined model for the case $\phi = 1$ for different gas mixtures and obstruction heights.

1 TU Munich unconfined model

```
#%% Import modules
from __future__ import print_function
from __future__ import division
import cantera as ct
import numpy as np
import matplotlib.pyplot as plt
import pandas as pd
from copy import deepcopy
import scipy
from scipy.optimize import fsolve
import os
import LFS as LFS

# Close all figures
plt.close('all')

# Set figure parameters
plt.style.use('default')
plt.rcParams['axes.labelsize'] = 14
plt.rcParams['xtick.labelsize'] = 12
plt.rcParams['ytick.labelsize'] = 12
plt.rcParams['legend.fontsize'] = 10
plt.rcParams['figure.figsize'] = (8,6)
plt.rcParams['figure.autolayout'] = True

blue_color = '#4285F4'
red_color = '#DB4437'
green_color = '#0F9D58'
yellow_color = '#F4B400'

# Reaction mechanism [Oconair]
mechanism_file_dir = os.getcwd() + '\\chem.cti'

# Inlet temperature in K and inlet pressure in pa
#In this case we are setting the inlet T and P to room temperature conditions
T_u = 293        # Inlet temperature in K
p_u = 101325     # Inlet pressure in Pa

# Define geometry: 'channel' or 'tube'
geometry = 'channel'
if geometry == 'channel':
    d_h = 31.5          # Hydraulic diameter in m
    d_h = d_h/1000      # Hydraulic diameter in mm
    h = 17.5/1000
    l_t = 0.5*h
```

```
elif geometry == 'tube':
    d_h = 25.2          # Hydraulic diameter in m
    d_h = d_h/1000      # Hydraulic diameter in mm
    h = d_h
    l_t = 1*h

# Define volume percentages of fuel
H2_percentage = 100  # Volume percentage of hydrogen in fuel
DNG_percentage = 100 - H2_percentage
CH4_percentage = 81.87 # Volume percentage of CH4 in DNG
C2H6_percentage = 3.73 # Volume percentage of C2H6 in DNG
N2_in_DNG_percentage = 100 - (CH4_percentage + C2H6_percentage)


# Define volume fractions of fuel
H2_fraction = H2_percentage/100
DNG_fraction = DNG_percentage/100
CH4_fraction = CH4_percentage/100
C2H6_fraction = C2H6_percentage/100

N2_in_DNG_percentage = 100 - (CH4_percentage + C2H6_percentage)
N2_in_DNG_fraction = N2_in_DNG_percentage/100
REST_in_DNG_percentage = 0

# Amount of moles for stoichiometric conditions
n_CH4 = 1/2
n_C2H6 = 2/7
n_H2 = 2

# Initialize vectors
phi_start = 0.35
phi_end = 1.00
phi_step = 0.05
phis = np.linspace(start=phi_start, stop=phi_end , num=1 + (phi_end-phi_start)/phi_step)
#phis = np.array([1.00])
U_FB = np.ones(len(phis))*10
L_M = np.zeros(len(phis))
S_l0 = np.zeros(len(phis))
alpha_fb_model= np.zeros(len(phis))
u_tau_model = np.zeros(len(phis))
u_fluc_yFB_model = np.zeros(len(phis))
kappa_local_model = np.zeros(len(phis))
kappa_global_model= np.zeros(len(phis))
S_ts_global_model = np.zeros(len(phis))

# Start iteration
for phi in range(0,len(phis)):
    gas = ct.Solution(mechanism_file_dir)

    gas.set_equivalence_ratio(phis[phi],{'H2':n_H2*H2_fraction},{'O2':1.0, 'N2':3.76})
    gas.transport_model= 'Multi'

    gas.TP = T_u, p_u
```

```
cp_u = gas.cp_mass
rho_u = gas.density_mass
mu_u = gas.viscosity
nu_u = mu_u/rho_u
lambda_u= gas.thermal_conductivity
alpha_u = lambda_u/(rho_u*cp_u)

# Domain width in metres
width = 0.004*2

# Create the flame object
flame = ct.FreeFlame(gas, width=width)

# Define tolerances for the solver
flame.set_refine_criteria(ratio=3, slope=0.1, curve=0.1)

# Define logging level
loglevel = 1

flame.solve(loglevel=loglevel, auto=True)
Su0 = flame.u[0]

T_b = gas.T
cp_b = gas.cp_mass
rho_b = gas.density_mass
mu_b = gas.viscosity
nu_b = mu_b/rho_b
S_l0[phi] = LFS.inter(phis[phi] , T_u , p_u*10**(-5))

print("Flame velocity: {:.2f} cm/s".format(Su0*100))
print("Unstretched laminar flame velocity: {:.2f} cm/s".format(S_l0[phi]*100))
print("Adiabatic flame temperature: {:.2f} K".format(T_b))
print("---------------------------------------------------------------------")

# Start with defining parameters for the TU Munich unconfined Model
sigma = rho_u/rho_b
gamma_1 = sigma
gamma_2 = 1

#Zel'dovich number
R_universal_gas = 1.987*10**(-3) #kcal/molK
E_a = 30 # kcal/mol
Ze = (E_a/R_universal_gas)*(T_b-T_u)/(T_b**2)

# Lewis numbers
Le_H2 = 0.33
Le_CH4 = 0.96
Le_C2H6 = 0.83
Le_O2 = 2.32

inbetween = CH4_fraction*Le_CH4 + C2H6_fraction*Le_C2H6
Le_fuel = H2_fraction*Le_H2 + DNG_fraction*inbetween
```

```
    B = 1 + Ze*((1/phis[phi]) - 1)
    Le = 1 + (Le_O2 - 1 + B*(Le_fuel -1))/(1 + B)

    #Markstein Length.
    delta_f = 2*lambda_u/(rho_u*cp_u*S_l0[phi])
    beta = gamma_1 + 0.5*Ze*(Le-1)*gamma_2
    L_M[phi] = delta_f*(beta-(sigma-1)*(gamma_1/sigma))

#%% Start of unconfined model
    C_s = 2.6

    G1 = 2.5
    G2 = 0.7
    G3 = -0.4

    s = np.log10(l_t/delta_f)

    # Law of the wall
    K = 0.41
    B = 5.0

    error = 10
    while error > 0.001:
        def equation1(eq1):
            u_tau = eq1
            if geometry == 'channel':
                return U_FB[phi]/u_tau - ((1/K)*np.log((h*u_tau/nu_u)) + B - (1/K))
            if geometry == 'tube':
                return u_tau - ( 0.03955*U_FB[phi]**(7/4)*nu_u**(1/4)*h**(-1/4))**0.5
        u_tau = (fsolve(equation1, 0.1, xtol=1.5e-3))

        # Local fluctuations
        u_fluc_yFB = 1.5*u_tau
        u_yFB = 11.38*u_tau # Waar komt deze elf vandaan!?

        # Local flame stretch rate
        Gamma_local = 10**(-1/(s+0.4)*np.exp(-(s+0.4)) +
        (1-np.exp(-(s+0.4)))*(2/3*(1-0.5*np.exp(-(u_fluc_yFB/S_l0[phi])**(1/3)))*s-0.11))
        kappa_local = (2/3)*Gamma_local*u_fluc_yFB/l_t + (1/2)*u_fluc_yFB/l_t

        # Local turbulent burning velocity
        S_ls_local = S_l0[phi] - L_M[phi]*kappa_local
        S_ts_local = S_ls_local*(1 + C_s*(u_fluc_yFB/S_ls_local)**0.5)

        # Global fluctuations
        u_fluc_B = 0.16*U_FB[phi]*(d_h*U_FB[phi]/nu_u)**(-1/8)
        u_fluc_global = u_fluc_B*(1 + G1*((S_l0[phi]/u_fluc_B)**G2))

        # Global flame stretch rate
        Gamma_global = 10**(-1/(s+0.4)*np.exp(-(s+0.4)) +
        (1-np.exp(-(s+0.4)))*
        (2/3*(1-0.5*np.exp(-(u_fluc_global/S_l0[phi])**(1/3)))*s-0.11))
        kappa_global = (2/3)*Gamma_global*u_fluc_global/l_t + (1/2)*u_fluc_global/l_t
```

```
        # Global turbulent burning velocity
        S_ls_global = S_l0[phi] - L_M[phi]*kappa_global
        S_ts_global = S_ls_global*(1 + C_s*(u_fluc_global/S_ls_global)**0.5)

        alpha_fb = np.arcsin(S_ts_local/u_yFB)
        U_FB_new = S_ts_global/np.sin(alpha_fb)
        error = abs((U_FB_new-U_FB[phi])/U_FB[phi])
        if error < 0:
            print('flashback is already occurring')
        U_FB[phi] = U_FB_new

    alpha_fb_model[phi] = alpha_fb*180/np.pi
    u_tau_model[phi] = u_tau
    u_fluc_yFB_model[phi] = u_fluc_yFB
    kappa_local_model[phi] = kappa_local
    kappa_global_model[phi] = kappa_global
    S_ts_global_model[phi] = S_ts_global

U_hoferichter_thesis = [[0.35, 4.95], [0.40, 5.87], [0.45, 6.67],
[0.50, 7.40], [0.55, 8.04], [0.60, 8.63], [0.65, 9.15], [0.70, 9.60], \
                        [0.75, 9.97], [0.80, 10.26], [0.85, 10.46],
                        [0.90, 10.57], [0.95, 10.57], [1.00, 10.47]]

phi_hoferichter, U_FB_hoferichter = zip(*U_hoferichter_thesis)




#%% Experimental data
viscosity = np.array([1.67, 1.67, 1.67, 1.67, 1.80, 1.80, 1.80, 1.80,
2.06, 2.06, 2.06, 2.06])*10**(-5)
u_rms = np.array([0.8, 0.84, 0.92, 0.98, 1.42, 1.5, 1.5, 1.58, 2.28, 2.4, 2.5, 2.55])
v_rms = np.array([1.66, 1.69, 1.69, 1.67, 2.70, 2.65, 2.55, 2.6, 4.63, 4.65, 4.68, 4.44])
alpha_f = np.array([10.5, 11.3, 12.1, 14.4, 12.4, 13.1, 13.9, 14.6,
15.8, 16.7, 16.7, 17.6])
U_FB_exp = np.array([5.07, 5.18, 5.58, 6.585, 8.19, 8.61, 9.57, 10.93,
14.32, 15.03, 17.22, 19.29])
S_l = np.array([1.43, 1.43, 1.43, 1.43, 1.89, 1.89, 1.89, 1.89, 2.35, 2.35, 2.35, 2.35])
u_fluc_exp_norm = np.array([1, 1.05, 1.15, 1.225, 1, 1.056, 1.056,
1.11, 1, 1.05, 1.096, 1.1184])
# rho en nu zoals in model
viscosity = np.array([4.32e-05, 4.32E-05, 4.32E-05, 4.32E-05,
4.32E-05, 4.32E-05, 4.32E-05, 4.32E-05, 4.32E-05, 4.32E-05, 4.32E-05, 4.32E-05])
rho = np.array([0.924, 0.924, 0.924, 0.924, 0.924, 0.924, 0.924,
0.924, 0.924, 0.924, 0.924, 0.924])
thermal_diffusivity = np.array([0.004607, 0.004607, 0.004607,
0.004607, 0.004607, 0.004607, 0.004607, 0.004607, 0.004607, 0.004607,
0.004607, 0.004607])


U_FB_exp = np.array([ 8.93 , 11.895, 14.26, 15.82 , 15.475])
phi_exp = np.array([0.60, 0.80, 1.00, 1.20, 1.40])
```

```
#%% Plots
phi_exp = np.array([0.60, 0.80, 1.00, 1.20, 1.40])
U_FB_exp_1 = np.array([ 8.93 , 11.895, 14.26, 15.82 , 15.475])
size = 11
plt.figure(1)
plt.plot(phis, U_FB, color=red_color, linestyle='None', marker='.',
label='TU Munich replicated, channel',markersize=size)
plt.plot(phis, U_FB_hoferichter, color=blue_color, linestyle='None',marker='*',
label='TU Munich, channel',markersize=size)
plt.xlabel('$\phi$ (-)')
plt.ylabel('$U_{FB}$ (m/s)')
plt.legend(prop={"size":11})
plt.grid()

# ---------------------------------------------------------------------------
u_rms = np.array([2.28, 2.4, 2.5, 2.55])
u_fluc_exp_norm = u_rms/u_rms[0]
alpha_fb_exp = np.array([15.8, 16.7, 16.7, 17.6])
alpha_fb_exp_norm = alpha_fb_exp/alpha_fb_exp[0]
U_FB_exp_H100 = np.array([14.258, 14.736, 16.286, 18.018])


plt.figure(2)
plt.plot(phis, u_tau_model, color=red_color, linestyle='None', marker='*', label='A')
plt.plot(phis, u_fluc_yFB_model, color=blue_color, linestyle='None',
marker='*', label='B')
# plt.scatter(phi_hoferichter, U_FB_hoferichter,
label='Hoferichter (unconfined), channel')
#plt.plot(phis, U_hoferichter,'*k',
label='Hoferichter, channel')
plt.xlabel('$\phi$ (-)')
plt.ylabel(r'$u_{\tau}$ (m/s)')
plt.grid()

plt.figure(3)
plt.plot(phis, u_tau_model, color=red_color, linestyle='None',
marker='*', label='A')
plt.plot(phis, u_fluc_yFB_model, color=blue_color, linestyle='None',
marker='*', label='B')
# plt.scatter(phi_hoferichter, U_FB_hoferichter,
label='Hoferichter (unconfined), channel')
#plt.plot(phis, U_hoferichter,'*k',
label='Hoferichter, channel')
plt.xlabel('$\phi$ (-)')
plt.ylabel(r'$u_{\tau}$ (m/s)')
plt.grid()
```

C Flame front location

Flame front location and angle are needed for the flashback prediction model used in the present research. Four methods to determine flame front location and flame angle were tested. Method 3 was used in the present research and is described in section 3.5.1. The other methods are discussed below.

Method 1

The method Faldella used to determine flame front location and flame angle corresponds to method 1 in the present research [Faldella, 2019]. The results in [Faldella, 2019] suggest that it is possible to determine flame angle with method 1. The underlying assumption in method 1 is that the radial coordinate of the flame front location at a particular axial station corresponds to the location where the intensity values of raw images of the PIV seeding particles equal the average value of the intensity values in burned and unburned gas regions, see Figure 5.1.

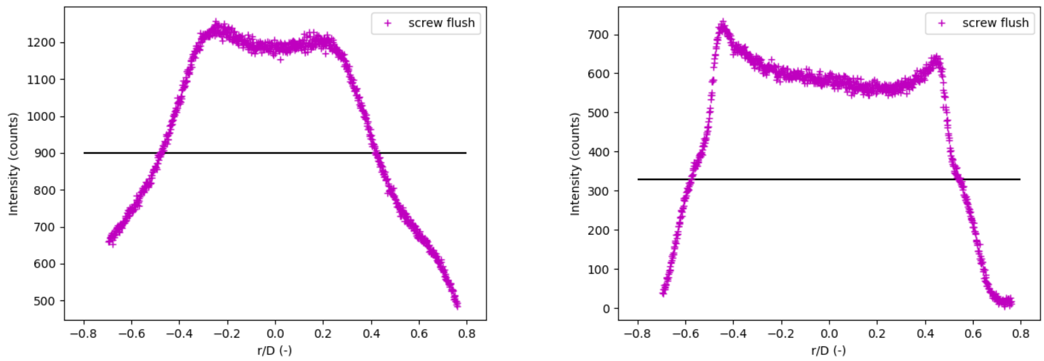

(a) Intensity values at a station 10 mm downstream the burner exit

(b) Intensity values at a station 3 mm downstream the burner exit

Figure 5.1: The high intensity values correspond to the zone with highest seeding density which, in turn, corresponds to the unburned gas. The black line marks the average intensity value. The radial location where the black line and the measured intensities intersect is set equal to the flame front location.

Figure 5.2 shows the effect of the obstruction h_{obstr} on the flame front location as determined with method 1.

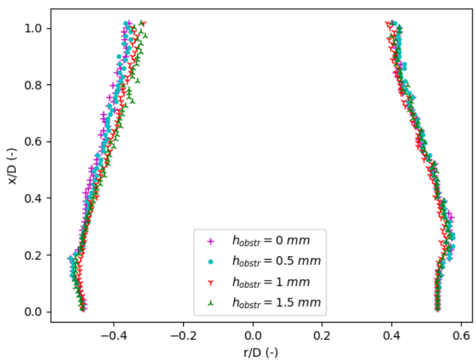

Figure 5.2: Flame front location as determined from method 1 for four values of the obstruction height. The experimental conditions: 60% H_2, Re = 10500, d_i = 25.20 mm, $U_b = 7.1$, ϕ = 1.

The curves in Figure 5.2 show that, for $r < 0$, the flame front axial distance from the burner rim decreases with increasing obstruction height. The Figure also shows that flame overhang is captured with this method. The drawback of this method is that the flame front plotted for $h_{obstr} = 0$ mm is not axisymmetric.

Method 2

The underlying assumption of method 2 is that the flame front location at a particular axial station corresponds to the location of the peak in RMS of the intensity of the raw PIV images.

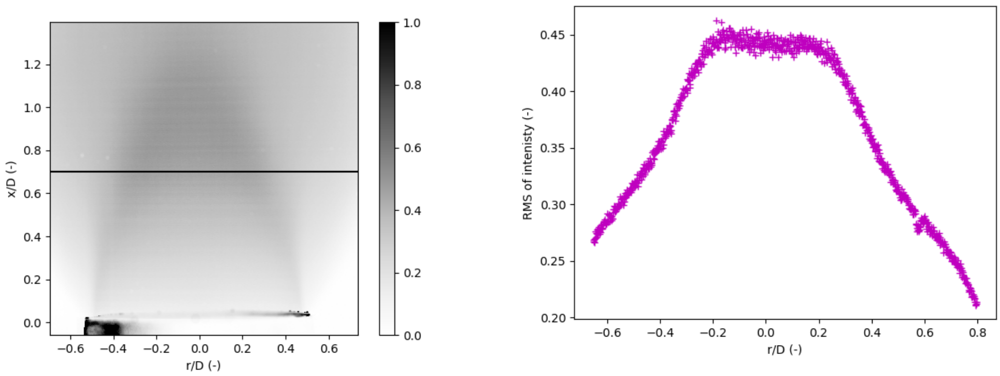

(a) RMS of intensity of the raw PIV images. *(b) RMS of intensity at a station 0.7 x/D the burner exit.*

Figure 5.3: The solid black line is the line $x/D = 0.7$. The figure on the right hand side shows that at a fixed axial station x/D = 0.7, RMS of intensity values of the flame front and the unburned flow are equal. The flame was produced by a tube burner with diameter d = 25.20 mm for the case 60% H_2. The equivalence ratio is $\phi = 1$, the Reynolds number is $Re = 10500$ and $h_{obstr} = 0$ mm.

Figure 5.3a shows that at a station $x/D = 0.7$ there is no clear peak in RMS of the intensity of the raw PIV images. Figure 5.4 shows the flame front location determined with method 2.

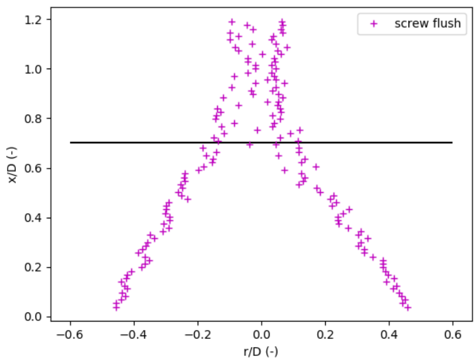

Figure 5.4: Flame front location determined from method 2 for the case $h_{obstr} = 0$ mm. The solid black line is the line $x/D = 0.7$.

Figure 5.4 shows the flame front location as obtained with method 2. It can be seen that at $x/D = 0.7$ the radial coordinate of the flame front is $r/D \approx 0$ and it seems the method tends to underpredict the true axial distance front flame front to burner rim.

Method 4

The underlying assumption of method 4 is that the flame front location at a particular axial station corresponds to the radial coordinate where the reacting flow field characteristics (mean velocity and Reynolds stresses) start to deviate qualitatively from the non-reacting flow field characteristics. Figure 5.5 plots the mean velocity in axial direction, the Reynolds normal stresses and the Reynolds shear stress 5 mm downstream the burner exit.

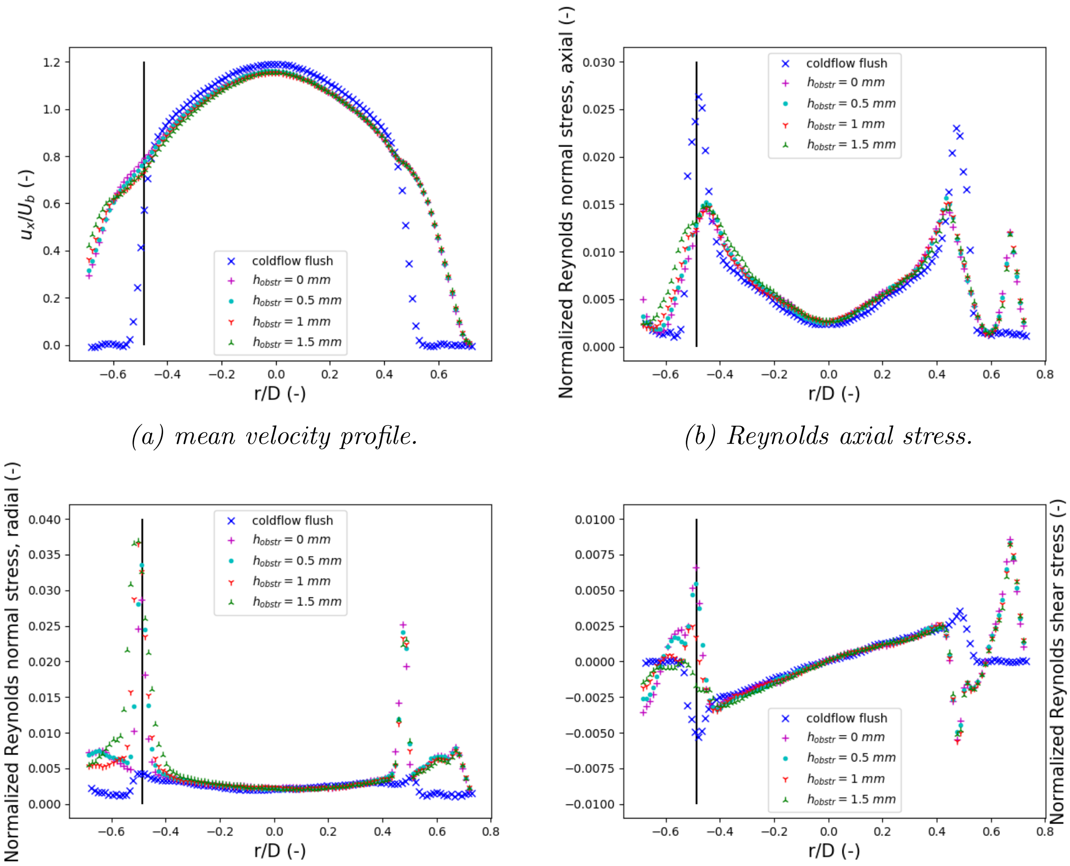

(a) mean velocity profile. *(b) Reynolds axial stress.*

(c) Reynolds radial stress. *(d) Reynolds shear stress.*

Figure 5.5: Flow characteristics 5 mm downstream the burner exit. The black line is the line $y^+ = 16.4$. The 60% H_2 flame was produced by a tube burner with diameter 25.20 mm. The Reynolds number is Re = 10500, $\phi = 1$. The experiment was cooled and the bulk velocity was 7.1 m/s.

In Figure 5.5 the results for the reacting flow field start to deviate from the cold flow results around $r/D = -0.47$ and $r/D = 0.50$. This followed from visual inspection of the results. In case of a boundary layer obstruction the flame front is located close to the central axis. That is: in Figure 5.5a it can be seen that the curve $h_{obstr} = 1.5$ mm deviates for smaller $|r|$ from curve 'coldflow' than curve $h_{obstr} = 0$ mm. The flow characteristics of three downstream locations were included in appendix E. The location of the flame fronts for different obstruction heights h_{obstr} as determined with method 4 is shown in Figure 5.6.

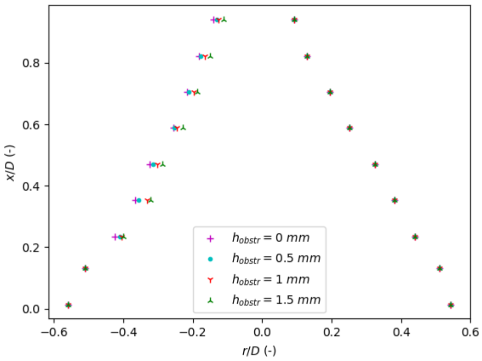

Figure 5.6: Flame front location determined from method 4 for four values of the obstruction height.

Figure 5.6 shows the flame fronts as determined with method 4. It can be seen that the flame fronts overlap for $r > 0$, but for $r < 0$, the flame front downstream distance from the burner rim decreases with screw tip height. The drawback of this method is that is it sensitive to human error.

Method 3: other cases

Method 3 was used to determine flame front location and flame angle. The 60% H_2 case is shown in Chapter 3, the 80 and 100% case are shown in Figure 5.7.

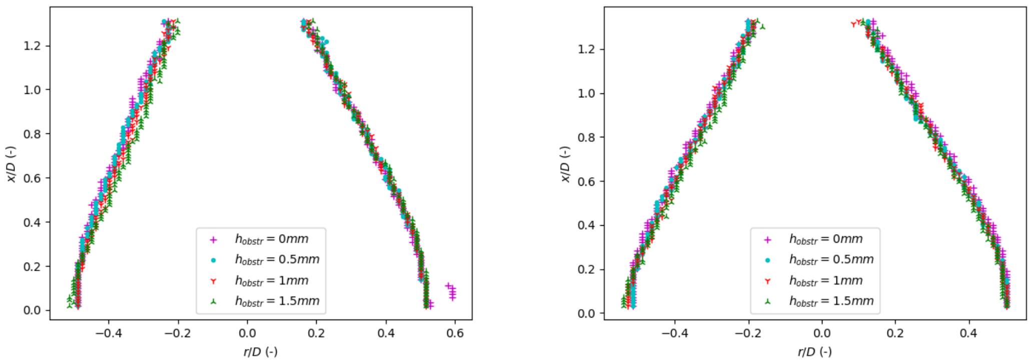

(a) 80% H_2 *(b) 100% H_2*

Figure 5.7: Flame fronts of 80 and 100% H_2 flames, modelled with method 3

D Flashback maps

1 Reproduction measurements

Figure 5.8b shows the flashback map as repeated in [Faldella, 2019]. Figure 5.8a shows a flashback map as determined in the present research for the same fuel/air mixtures as reported in Faldella's work. The set-up was the same except burner diameter. The names in the figure legend are equal to the volumetric percentage hydrogen in the fuel. Hydrogen, DNG and mixtures are used as fuel. The fuel/air mixtures studied contain 0, 20, 40, 60, 80 and 100% H_2.

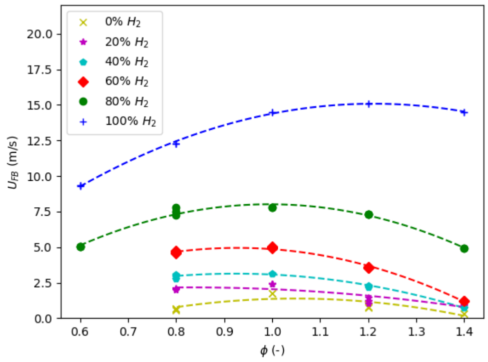

(a) Flashback map for six fuel/air mixtures as determined in the present research. Burner diameter is d = 19.76 mm for all fuel mixtures.

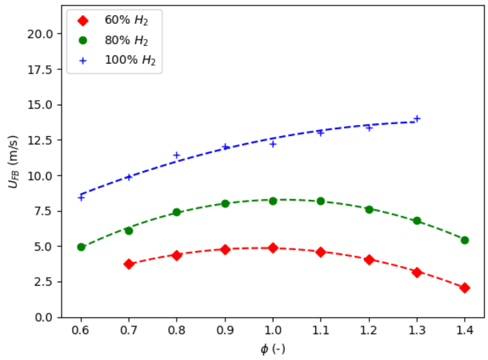

(b) flashback map as reported by Faldella [Faldella, 2019]. Burner diameter is d = 39.40, 25.67, and 20.06 mm for the 60, 80 and 100% H_2 cases, respectively.

Figure 5.8: Flashback map to compare with Faldella's work. Both burners were cooled during experiments. Faldella did not report data sets of cooled 0, 20, and 40% H_2 cases. Figure 5.8a is the reference case and identical to Figure 4.1.

Figure 5.8a and Figure 5.8b correspond qualitatively. However the 100% H_2 data set obtained in the present research is higher than the data set reported in [Faldella, 2019] with a maximum difference of 15% at $\phi = 1$.

E Flow characteristics

Flow characteristics 1, 5 and 10 mm downstream the burner exit for the cases 60, 80 and 100% H_2 for different obstruction heights.

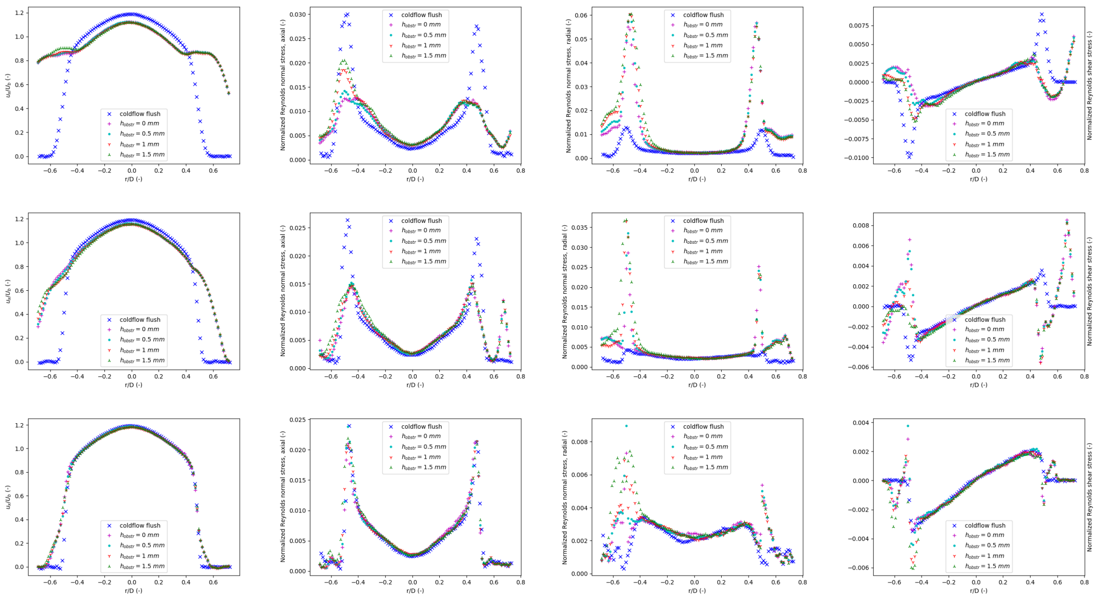

Figure 5.9: Top to bottom: Flow characteristics at 10, 5 and 1 mm downstream the burner exit. Left to right: Normalized mean velocity, normalized Reynolds normal stress in axial direction, normalized Reynolds normal stress in radial direction and normalized Reynolds shear stress. All Figures are shown for the case 60% H_2, Re = 10500, ϕ = 1 and d = 25.20 mm.

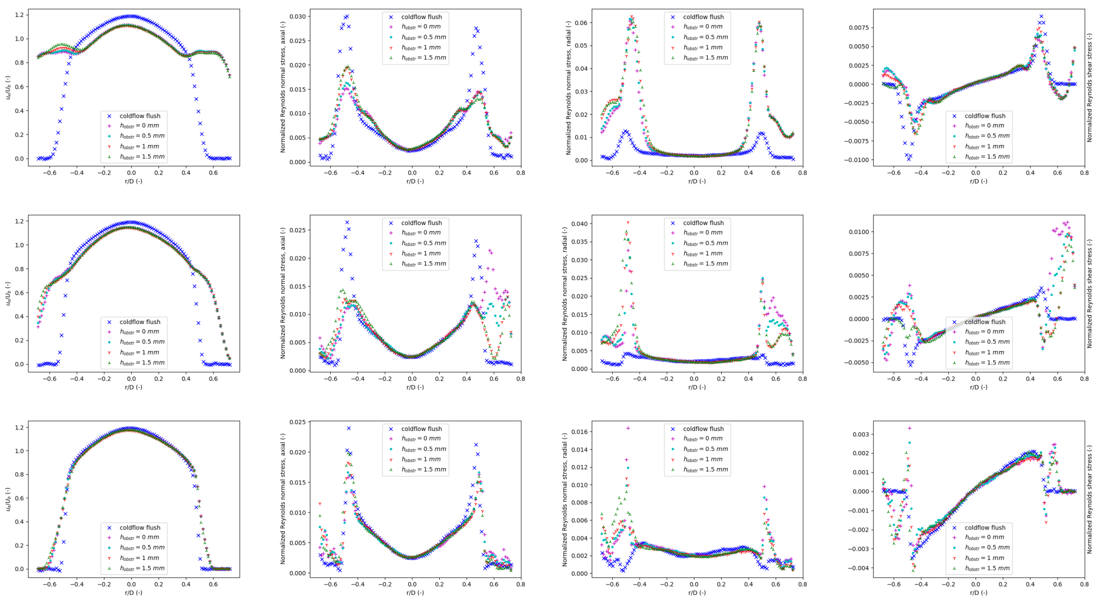

Figure 5.10: Top to bottom: Flow characteristics at 10, 5 and 1 mm downstream the burner exit. Left to right: Normalized mean velocity, normalized Reynolds normal stress in axial direction, normalized Reynolds normal stress in radial direction and normalized Reynolds shear stress. All Figures are shown for the case 80% H_2, Re = 15800, ϕ = 1 and d = 25.20 mm.

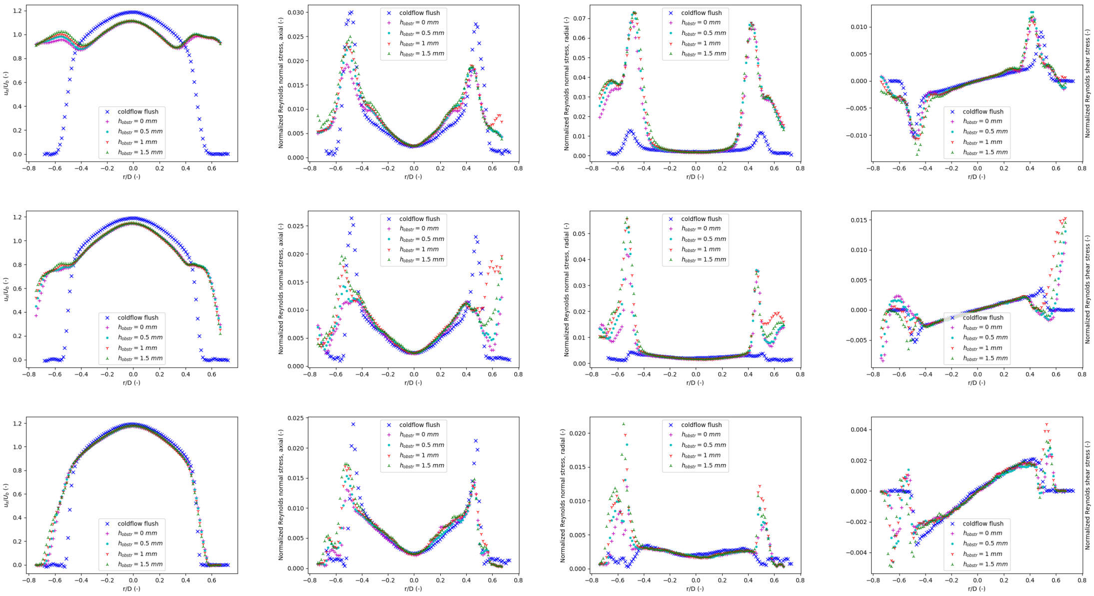

Figure 5.11: Top to bottom: Flow characteristics at 10, 5 and 1 mm downstream the burner exit. Left to right: Normalized mean velocity, normalized Reynolds normal stress in axial direction, normalized Reynolds normal stress in radial direction and normalized Reynolds shear stress. All Figures are shown for the case 100% H_2, Re = 23400, $\phi = 1$ and d = 25.20 mm.

F Histograms

In this section all histograms showing any effect of the obstruction height on the velocity distribution are shown. The histogram in 5.12d does not show any effect of obstruction height on velocity distribution and might be used as reference case.

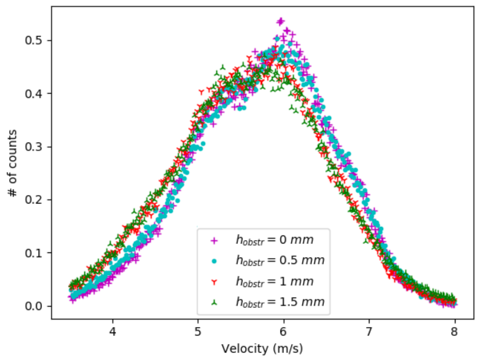

(a) histogram 6 mm downstream the burner rim for the case 60% H_2.

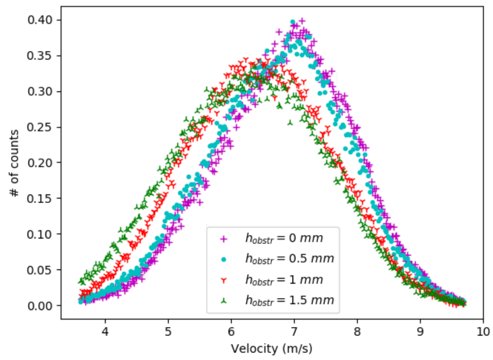

(b) histogram 3 mm downstream the burner rim for the case 80% H_2.

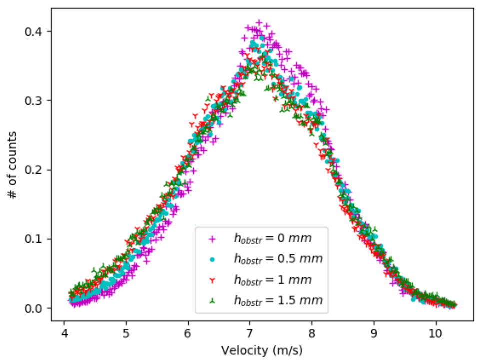

(c) histogram 3 mm downstream the burner rim for the case 100% H_2.

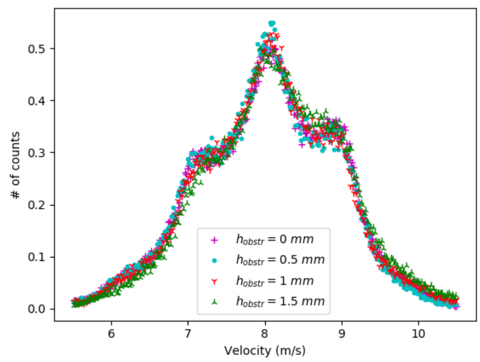

(d) histogram 12 mm downstream the burner rim for the case 80% H_2

Figure 5.12: Figures 5.12a, 5.12b and 5.12c show the rest of the histograms that indicate that BL obstruction influences the velocity. Figure 5.12d shows how the histograms look if obstruction height does not influence the velocity. Thirteen histograms were made, twelve downstream the BL obstruction, one on the other end of the burner rim. Only four histograms showed a dependence of velocity on obstruction height. The other nine look like Figure 5.12d.

G Labview

1 Frontpanel Labview

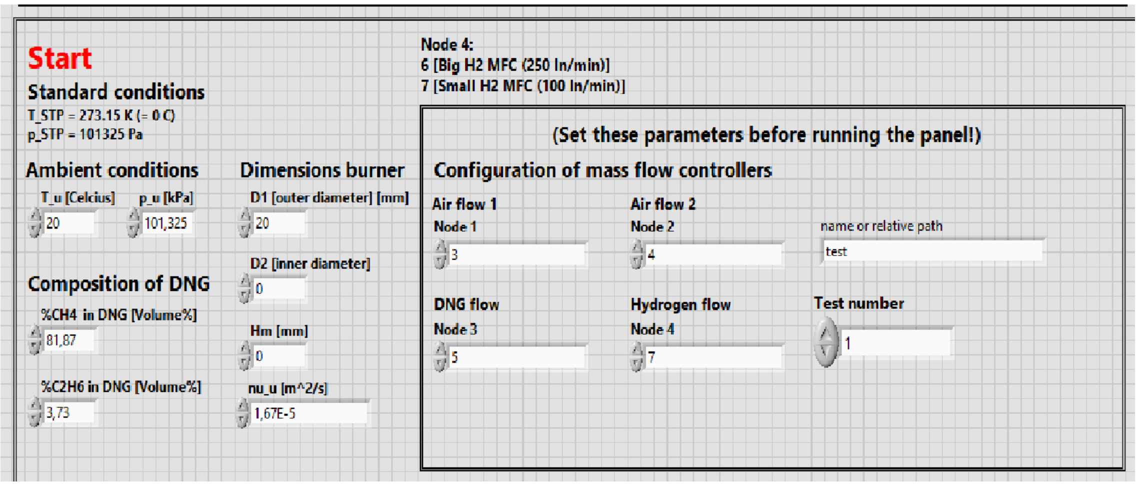

(a) Initial conditions, to set at the beginning of each experiment.

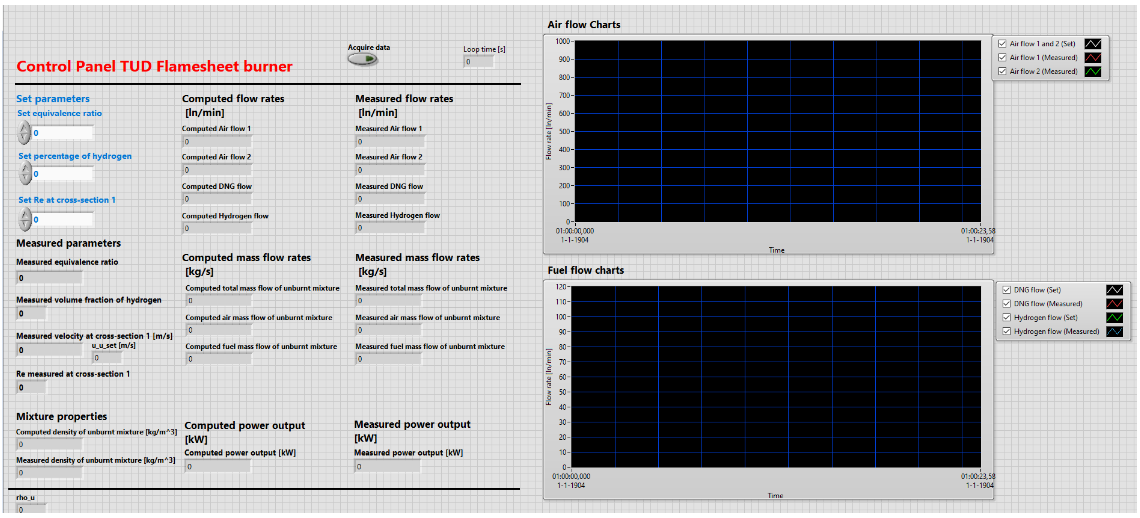

(b) Live conditions. The three boxes in the top left corner are the input for the MFC. The second and third column show the computed and measured flow rates, respectively. The front panel continuously shows the measured and computed flow rate, volume fraction of hydrogen and equivalence ratio. The measured and computed values were compared during experiments to make sure that experiments were not influenced by differences in measured and computed values caused by poor convergence of a MFC.

Figure 5.13

2 Labview backpanel: Governing equations

The Labview panel was designed by Luuk Altenburg, so the following section is his work.

Molar Masses and molar volume

$$M_H = 1.008\frac{g}{mole}; \quad M_{H2} = 2M_H; \quad M_C = 12.011\frac{g}{mole}; \quad M_n = 14.007\frac{g}{mole};$$

$$M_{N2} = 2M_N; \quad M_O = 15.999\frac{g}{mole}; \quad M_{O2} = 2M_O; \quad M_{Ar} = 39.948\frac{g}{mole};$$

$$R_{gas} = 8.314\frac{PaM^3}{moleK}; \quad V_m = \frac{R_{gas}T}{P}$$

Density of species

$\rho_{H2} = \frac{2M_H}{V_m}; \quad \rho_{CH4} = \frac{M_C + 4M_H}{V_m};$

$\rho_{C2H6} = \frac{2M_C + ^m_H}{V_m}; \quad \rho_a = \frac{f_{N2/air}M_{N2} + f_{O2/air}M_{O2} + f_{Ar/air}M_{Ar}}{V_m}$

Composition of air

Volume fractions: $f_{N2/air} = 0.78; \quad f_{O2/air} = 0.21; \quad f_{Ar/air} = 0.01$

Number of moles of air normalized for 1 mole O_2:
$n_a = \frac{f_{N2/air}}{f_{O2/air}} + \frac{f_{O2/air}}{f_{O2/air}} + \frac{f_{Ar/air}}{f_{O2/air}} = \frac{f_{N2/air}}{f_{O2/air}} + 1 + \frac{f_{Ar/air}}{f_{O2/air}} = 4.76$

$n_a AIR = \frac{f_{N2/air}}{f_{O2/air}} N_2 + 1O_2 + \frac{f_{Ar/air}}{f_{O2/air}} Ar$

Composition of fuel

$x_{DNG} + x_{H2} = 1; \quad x_{CH4} + x_{C2H6} + x_{N2} = x_{DNG}$

$x_{CH4} = 0.8187x_{DNG}; \quad x_{C2H6} = 0.0373x_{DNG}; \quad x_{N2} = 1 - (x_{CH4} + x_{C2H6})$

Chemical reactions

Combustion of hydrogen:

$x_{H2}\Big(H_2 + 0.5n_{air} \rightarrow H_2O + 0.5(\frac{f_{N2/air}}{f_{O2/air}N_2} + \frac{f_{Ar/air}}{f_{O2/air}})\Big)$

Combustion of Methane:

$x_{CH4}\Big(CH4 + 2n_a AIR \rightarrow CO_2 + H_2O + 2(\frac{f_{N2/air}}{f_{O2/air}}N_2 + \frac{f_{Ar/air}}{f_{O2/air}}Ar)\Big)$

Combustion of ethane:

$x_{C2H6}\Big(C_2H_6 + 3.5n_a AIR \rightarrow 2CO_2 + 3H_2O + 3.5(\frac{f_{N2/air}}{f_{O2/air}}N_2 + \frac{f_{Ar/air}}{f_{O2/air}}Ar)\Big)$

Correction for Standard Temperature and Pressure (STP)

$T_{STP} = 273.15K; \quad p_{STP} = 101325Pa$

Ideal Gas Law:

$pV = nRT \rightarrow pQt = nRT$

Unburned conditions:

$\frac{p_u Q_x}{RT_u} = \frac{p_{STP}Q_{x.STP}}{RT_{STP}} \rightarrow Q_x = Q_{x,STP}\frac{T_u}{T_{STP}}\frac{p_{STP}}{p_u}$

$\phi = \frac{\dot{m}_f/\dot{m}_a}{(\dot{m}_f/\dot{m}_a)_{stoich}} = \frac{Q_f/Q_a}{(Q_f/Q_a)_{stoich}} = \frac{n_f/n_a}{(n_f/n_a)_{stoich}}$

for $n_{f,stoich} = 1 \rightarrow (n_f/n_a)_{stoich} = \frac{1}{n_a(0.5x_{H2} + 2x_{CH4} + 3.5x_{C2H6})}$

Flow rates and velocity

$Q_u = Q_a + Q_f; \quad Q_u = Au_u$

$Q_f = \frac{u_u A}{1+1/(\phi(n_f/n_a)_{stoich})}; \quad Q_a = \frac{u_u A}{1+\phi(n_f/n_a)_{stoich}}$

$\dot{m}_u = \dot{m}_a + \dot{m}_f; \quad \dot{m}_f = \rho_u + Q_u$

$\dot{m}_f = \rho_f Q_f; \quad \dot{m}_a = \rho_a Q_a$

$\rho_u = \frac{\rho_f Q_f + \rho_a Q_a}{Q_u}$

$\rho_f = \rho_{H2} x_{H2} + \rho_{CH4} x_{CH4} + \rho_{C2H6} x_{C2H6}$

H Dutch Natural Gas composition

Mole percentage Dutch Natural Gas (%)	
CH_4	81.27
N_2	14.44
C_2H_6	3.73
Rest	0.56
Mole percentage air (%)	
N_2	78
O_2	21
Ar	1

Table 5.1: Composition Dutch Natural Gas and air